Geochemistry, Geophysics, Geosystems

RESEARCH ARTICLE
10.1029/2018GC008060

# Role of Large-Scale Tectonic Forces in Intraplate Earthquakes of Central and Eastern North America

**Attreyee Ghosh[1], William E. Holt[2], and Alireza Bahadori[2]**

[1]Centre for Earth Sciences, Indian Institute of Science, Bangalore, India, [2]Department of Geosciences, Stony Brook University, Stony Brook, NY, USA

**Key Points:**
- GPE gradients and coupling with large-scale mantle flow generate stresses responsible for intraplate earthquakes in North America
- Intraplate strain rates in CEUS are dominated by GIA, but those associated with tectonic effects are unlikely to exceed 1 x $10^{-9}$ $year^{-1}$
- First-order strength contrasts in the lithosphere are needed to satisfy stress and strain indicators from earthquakes

**Correspondence to:**
A. Ghosh,
aghosh@iisc.ac.in

**Citation:**
Ghosh, A., Holt, W. E., & Bahadori, A. (2019). Role of large-scale tectonic forces in intraplate earthquakes of central and eastern North America. *Geochemistry, Geophysics, Geosystems*, *20*. https://doi.org/10.1029/2018GC008060

Received 5 NOV 2018
Accepted 15 MAR 2019
Accepted article online 20 MAR 2019

**Abstract** Central and eastern United States (CEUS) have experienced large intraplate earthquakes. Yet, at present there is no comprehensive model to explain stresses, strain, and seismicity in this intraplate setting. Models to explain the intraplate stresses in CEUS include glacio-isostatic adjustment, ridge push effects, local stresses along preexisting fracture zones, and large-scale convection. In this paper, we present a self-consistent model of the dynamics of CEUS that explains the stress field responsible for these intraplate earthquakes. The earthquakes represent slow, ongoing deformation associated with forces arising from a combination of lithosphere topography and structure, together with the effects of density-driven mantle flow. Using GPS data, we calculate strain rates that are likely to arise from tectonic effects and conclude that intraplate strain rates associated with tectonic effects are unlikely to exceed $1 \times 10^{-9}$ $year^{-1}$. We test several models of lateral viscosity variations by comparing model stress orientation output with earthquake moment tensors, $SH_{max}$ directions from stress inversion, and $P$ axes of earthquakes. A model that satisfies stress and earthquake constraints and also strain rate magnitude constraints requires high viscosity ($10^{25}$ Pa·s) craton and old oceanic lithosphere of the western Atlantic block and weaker ($5 \times 10^{24}$ Pa·s) accreted Appalachian terrane. Other strength contrasts within the lithosphere are likely present. Incorporation of these into future models using constraints from seismology, along with refined geodetic measurements and improved estimates of crust and upper mantle densities, is needed to further refine long-term dynamic models and better evaluate the hazards associated with this very slow, ongoing permanent deformation within the eastern and central United States.

## 1. Introduction

Although central and eastern North America constitute an intraplate setting, several large earthquakes have occurred there over the past three centuries (Bent, 1995, 1996; Du et al., 2003; Ebel, 2009; Horner et al., 1978; Horton et al., 2005; Hough & Page, 2011; Kim, 2003; Kim & Chapman, 2005; Kim et al., 2006; Ma et al., 2008; Neely et al., 2018; Sbar et al., 1975; Yang & Aggarwal, 1981). Most notable are the New Madrid earthquakes and their aftershocks that shook the Midwest between 1811 and 1812 and the 1886 Charleston earthquake in South Carolina. The 2011 Mineral, Virginia, M5.8 earthquake is a reminder that intraplate stresses continue to produce events of permanent strain within the plate interior (Horton et al., 2015; Wolin et al., 2012). Since the 2011 event, several other M3 and M4 events have occurred within the central and eastern United States (CEUS; Table 1). These earthquakes are not only confined to North America; several other regions of the world have witnessed large intraplate events (cf. Gangopadhyay & Talwani, 2003; Schulte & Mooney, 2005). These seismic events are in contrast to the fundamental principle of plate tectonics, which suggests that deformation takes place mainly at plate boundaries and boundary zones, whereas plate interiors remain undeformed (Wilson, 1965). A fundamental understanding of these earthquakes is crucial for a better assessment of seismic hazard. Although there is a general agreement that some of these earthquakes occur along favorably oriented ancient rifts (Schulte & Mooney, 2005; Stein et al., 1989; Sykes, 1978; Zoback & Richardson, 1996) and other major strength contrasts (Gallen & Thigpen, 2018; Mooney et al., 2012), there is no consensus on the sources of intraplate deformation and earthquakes. The intraplate events in North America have been variously attributed to glacial isostatic adjustment (GIA; Mazzotti et al., 2005; Muir-Wood, 2000), ridge push effects (Zoback & Zoback, 1981, 1980), dynamics of fault interaction (Liu & Stein, 2016), mantle weakening due to rifting or a plume event (Chen et al., 2016), gravitational body

**Table 1**
*Earthquake Data From Various Sources*

| Name | Year | Latitude | Longitude | Strike | Dip | Rake | Depth (km) | Magnitude | Reference |
|---|---|---|---|---|---|---|---|---|---|
| North Atlantic | 1978 | 30.04 | −67.57 | 318 | 32 | 73 | 15 | Mw = 6.2 | Global CMT |
| Kentucky | 1980 | 38.20 | −84.79 | 203 | 90 | 180 | 15 | Mw = 5.0 | Global CMT |
| New Brunswick | 1982 | 46.87 | −66.41 | 202 | 61 | 129 | 10 | Mw = 5.5 | Global CMT |
| New Brunswick | 1982 | 47.24 | −66.44 | 190 | 44 | 121 | 15 | Mw = 5.0 | Global CMT |
| New York | 1983 | 44.53 | −74.61 | 183 | 68 | 98 | 28.3 | Mw = 4.9 | Global CMT |
| Ohio | 1986 | 41.64 | −81.11 | 21 | 84 | 161 | 15.0 | Mw = 5.0 | Global CMT |
| Southern Quebec | 1988 | 48.01 | −71.16 | 189 | 39 | 135 | 27.5 | Mw = 5.8 | Global CMT |
| New York | 2002 | 44.65 | −73.51 | 162 | 75 | 90 | 15.0 | Mw = 5.1 | Global CMT |
| Southern Indiana | 2008 | 38.49 | −87.86 | 205 | 89 | 178 | 26.9 | Mw = 5.4 | Global CMT |
| Southern Indiana | 2008 | 38.48 | −87.91 | 214 | 85 | 174 | 21.8 | Mw = 4.8 | Global CMT |
| Southern Ontario | 2010 | 45.97 | −75.58 | 152 | 49 | 82 | 22.6 | Mw = 5.2 | Global CMT |
| Virginia | 2011 | 37.91 | −77.93 | 21 | 41 | 101 | 12.0 | Mw = 5.7 | Global CMT |
| Temiskaming, PA | 2000 | 46.87 | −78.90 | 116 | 68 | 69 | 13 | Mw = 4.6 | Du et al. (2003) |
| Pymatuning, PA | 1998 | 41.50 | −80.39 | 9 | 69 | 144 | 2 | Mw = 4.5 | Du et al. (2003) |
| La Conception, Canada | 1998 | 46.2 | −72.7 | 150 | 27 | 75 | 12 | Mw = 3.7 | Du et al. (2003) |
| Gaspe Peninsula, Canada | 1999 | 49.65 | −66.39 | 30 | 63 | 93 | 0 | Mw = 4.4 | Du et al. (2003) |
| Ashtabula, Ohio | 2001 | 41.99 | −80.83 | 5 | 79 | 159 | NA | Mw = 3.9 | Du et al. (2003) |
| Quebec City | 1997 | 46.75 | −71.35 | 39 | 63 | 87 | NA | Mw = 4.5 | Du et al. (2003) |
| Christieville | 1997 | 45.81 | −74.19 | 96 | 33 | 60 | NA | Mw = 3.6 | Du et al. (2003) |
| Charlevoix, Canada | 1997 | 47.67 | −69.91 | 27 | 66 | 111 | NA | Mw = 4.3 | Du et al. (2003) |
| Berlin, NH | 1996 | 44.18 | −71.35 | 144 | 60 | 93 | NA | Mw = 3.4 | Du et al. (2003) |
| Lachute, Canada | 1996 | 45.99 | −74.43 | 136 | 36 | 98 | NA | Mw = 3.7 | Du et al. (2003) |
| Lisbon, NH | 1995 | 44.29 | −71.91 | 95 | 50 | 40 | NA | Mw = 3.7 | Du et al. (2003) |
| Reading, PA | 1994 | 40.34 | −76.05 | 159 | 48 | 102 | NA | Mw = 4.6 | Du et al. (2003) |
| Napierville, Canada | 1993 | 45.20 | −73.46 | 144 | 45 | 96 | NA | Mw = 3.9 | Du et al. (2003) |
| Mont-Laurier, Canada | 1990 | 46.47 | −75.59 | 141 | 42 | 90 | NA | Mw = 4.6 | Du et al. (2003) |
| Grand Banks, Canada | 1929 | 44.69 | −56.0 | 122 | 74 | 140 | NA | Mw = 7.1 | Bent (1995) |
| Cornwall-Massena, Canada | 1944 | 44.96 | −74.72 | 313 | 70 | 52 | 20 | Mw = 5.8 | Bent (1996) |

forces (Levandowski et al., 2016, 2017), or large-scale convection (Forte et al., 2007). The role of GIA in reactivating these faults by perturbing the background stress has been proposed in relation to the 1929 Grand Banks (M7.2) and the 1933 Baffin Bay (Mw7.4) events (Bent, 1995, 2002). However, GIA effects diminish exponentially away from the margin of the ice sheet, and hence, they have been argued to play a minimal role south of the hinge line (James & Bent, 1994; Kreemer et al., 2018; Wu & Johnston, 2000). Recent studies have also argued that dynamic topography resulting from radial mantle flow impact the occurrence of earthquakes away from plate boundary (Becker et al., 2015; Forte et al., 2010).

Li et al. (2007) calculated Coulomb stresses likely to arise from the presence of a lithosphere-craton boundary and found that regions of high Coulomb stress correlated with seismically active regions in CEUS, indicating that lateral variations of lithospheric structure is important for the occurrence of seismicity in the CEUS. They also suggested that the transition between the thick North American craton and the surrounding lithosphere could concentrate stress along the margins of the craton, thus affecting seismicity. In another study, Mooney et al. (2012) found a correlation between seismicity and seismic velocity of the lithosphere at 175-km depth. They demonstrated that globally, cratonic lithosphere has fewer earthquakes than normal lithosphere, which they attributed to the greater strength of the cratons.

In this paper, we quantify the roles of lithospheric structure and surface topography jointly with global coupling between lithosphere and global mantle flow, the latter of which produces basal tractions. These tractions act at the base of the lithosphere (thin sheet model) as boundary condition to produce effective body forces. These effective body forces, along with the body forces arising from lithosphere structure and

**Table 1** *(continued)*

| Name | Year | Latitude | Longitude | Strike | Dip | Rake | Depth (km) | Magnitude | Reference |
|---|---|---|---|---|---|---|---|---|---|
| Caborn, IN | 2002 | 37.99 | −87.77 | 28 | 82 | −174 | 18 | Mw = 4.5 | Kim (2003) |
| Central Virginia | 2003 | 37.77 | −78.10 | 66 | 34 | 141 | 10 | Mw = 4.2 | Kim and Chapman (2005) |
| Lake Ontario | 2004 | 43.67 | −78.23 | 8 | 59 | 165 | 4 | Mw = 3.1 | Kim et al. (2006) |
| Bardwell, Kentucky | 2003 | 36.87 | −89.01 | 251 | 70 | 165 | 1 | Mw = 4.0 | Horton et al. (2005) |
| Kapuskasing, Canada | 2006 | 49.51 | −81.54 | 148 | 46 | 84 | 16 | Mw = 4.2 | Ma et al. (2008) |
| New Madrid | 1812 | 36.58 | −89.59 | 155 | 30 | 90 | NA | Mw = 7.7 | Hough (2004) |
| Sharpsburg, Kentucky | 1989 | 38.17 | −83.91 | 30 | 60 | 180 | 18 | Mw = 5.2 | Kim et al. (2006) |
| Western Maryland | 2010 | 39.17 | 77.25 | 325 | 45 | 50 | 18 | Mw = 3.4 | SLU |
| Central Alabama | 2009 | 33.01 | −87.14 | 275 | 85 | −10 | 5 | Mw = 3.8 | SLU |
| Bar Harbor, ME | 2006 | 44.33 | 68.17 | 340 | 35 | 85 | 2 | Mw = 3.9 | SLU |
| Quebec, Canada | 2005 | 44.68 | −80.48 | 320 | 25 | 65 | 10 | Mw = 3.6 | SLU |
| Western North Carolina | 2005 | 35.88 | −82.80 | 90 | 60 | −60 | 8 | Mw = 3.7 | SLU |
| Saranac Lake, NY | 2000 | 43.95 | 74.25 | 150 | 54 | 120 | 8 | Mw = 3.6 | SLU |
| Attica, NY | 1967 | 42.9 | −78.2 | 13 | 71 | 159 | 3 | mb = 4.4 | Zoback (1992) |
| St. Donat, Canada | 1978 | 46.3 | 74.1 | 156 | 51 | 84 | 7 | mb = 4.1 | Zoback (1992) |
| Goodnow, NY | 1983 | 43.94 | −74.26 | 180 | 60 | 81 | 7.5 | mb = 5.1 | Zoback (1992) |
| St. Francois, Missouri | 1965 | 37.5 | −91.0 | 260 | 40 | −71 | 5 | mb = 4.9 | Zoback (1992) |
| West Virginia | 1969 | 37.4 | −81.0 | 32 | 80 | 19 | 5 | mb = 4.6 | Zoback (1992) |
| Illinois Basin | 1965 | 37.2 | −89.3 | 280 | 70 | −20 | 1.5 | mb = 3.8 | Zoback (1992) |
| Mississippi | 1965 | 33.6 | −90.9 | 292 | 70 | 10 | 1.5 | mb = 4.5 | Zoback (1992) |
| Bowman, SC | 1972 | 33.31 | −80.58 | 259 | 40 | 9 | 2 | mb = 4.5 | Zoback (1992) |
| Missouri | 2018 | 36.2 | −89.7 | 11.2 | 110 | 70 | 5 | Mw = 3.6 | SLU |
| Ontario, Canada | 2018 | 42.1 | −83.0 | 5 | 120 | 75 | 20 | Mw = 3.3 | SLU |
| Delaware | 2017 | 39.2 | −75.4 | 8.1 | 100 | 60 | 25 | Mw = 4.2 | SLU |
| Quebec, Canada | 2015 | 49.42 | −66.79 | 335 | 60 | 70 | 10 | Mw = 3.8 | SLU |
| Missouri | 2015 | 36.05 | −89.82 | 110 | 85 | 10 | 10.9 | Mw = 4.0 | SLU |

topography, act on a plate with a specific effective viscosity structure to generate stress magnitudes and associated long-term strain rates. We further test the role of first-order lateral viscosity variations in the lithosphere and compare predictions of stress and strain rate patterns with seismicity and geodetic observations. We use earthquake *P* axes, earthquake moment tensors, and earthquake-inversion stresses to constrain our results. Additionally, we use GPS observations as a constraint on the lower bound for effective viscosity, which has implications for the maximum long-term moment rates that accommodate long-term deformation across this intraplate tectonic region. We emphasize that we are not addressing the question of specific occurrence of earthquakes, including the exact location and timing. What we are arguing is that stresses from large-scale tectonic forces (gravitational potential energy (GPE) plus coupling with mantle flow), which act on a lithosphere containing lateral effective viscosity variations, may create spatial variations in long-term strain rates and therefore long-term earthquake rates. We test only large-scale viscosity contrasts associated with first-order lithosphere variations, but we argue that future refinements can be achieved through the incorporation of new, higher-resolution constraints on lithosphere structure and smaller-scale lithosphere heterogeneities.

## 2. Method

### 2.1. Stresses Resulting From Topography and Large-Scale Mantle Flow

The origin of the lithospheric stress field can be attributed to two principal sources: (1) GPE differences that arise due to lateral density variations within the lithosphere along with topography variations and (2) horizontal tractions at the base of the lithosphere arising from density-driven mantle convection. These two influences combine with each other to produce a deviatoric stress field that causes deformation within the lithosphere (cf. Finzel et al., 2015; Ghosh, Becker, & Humphreys, 2013; Lithgow-Bertelloni & Guynn, 2004; Wang et al., 2015). We calculate these two contributions by solving the force-balance equations globally using

**Table 1** *(continued)*

| Name | Year | Latitude | Longitude | Strike | Dip | Rake | Depth (km) | Magnitude | Reference |
|---|---|---|---|---|---|---|---|---|---|
| Alabama | 2015 | 32.97 | −88.05 | 120 | 75 | 5 | 5 | Mw = 3.8 | SLU |
| Nova Scotia | 2015 | 44.12 | −66.29 | 140 | 65 | 55 | 5 | Mw = 3.4 | SLU |
| Missouri | 2015 | 36.77 | −90.85 | 125 | 85 | 20 | 17.6 | Mw = 3.4 | SLU |
| South Carolina | 2014 | 33.8 | −82.1 | 310 | 55 | 30 | 4.6 | Mw = 4.1 | SLU |
| Virginia | 2014 | 37.53 | −78.07 | 9.9 | 340 | 45 | 60 | Mw = 3.1 | SLU |
| Alabama | 2014 | 32.95 | −88.02 | 120 | 80 | −5 | 5.0 | Mw = 3.7 | SLU |
| Arkansas | 2013 | 35.62 | −90.54 | 315 | 75 | −5 | 5.0 | Mw = 3.7 | SLU |
| Quebec | 2013 | 45.75 | −76.34 | 135 | 50 | 65 | 14.5 | Mw = 4.5 | SLU |
| Quebec | 2013 | 49.80 | −66.07 | 135 | 50 | 60 | 5 | Mw = 4.0 | SLU |
| Virginia | 2012 | 37.95 | −77.98 | 195 | 20 | 60 | 3.0 | Mw = 3.1 | SLU |
| Missouri | 2012 | 36.85 | −89.41 | 150 | 45 | 25 | 5.0 | Mw = 4.0 | SLU |
| Virginia | 2012 | 37.91 | −77.98 | 175 | 60 | 55 | 7.4 | Mw = 3.0 | SLU |
| Maine | 2012 | 43.61 | −70.66 | 180 | 30 | 100 | 5.0 | Mw = 4.0 | SLU |
| Missouri | 2012 | 36.85 | −89.41 | 150 | 45 | 25 | 5.0 | Mw = 4.0 | SLU |
| Ontario | 2011 | 45.57 | −74.55 | 320 | 75 | 75 | 18.0 | Mw = 3.5 | SLU |
| Missouri | 2011 | 38.12 | −90.93 | 100 | 80 | 25 | 5.0 | Mw = 3.9 | SLU |
| Virginia | 2011 | 37.91 | −77.95 | 185 | 35 | 60 | 7.0 | Mw = 3.8 | SLU |
| New York | 2011 | 44.70 | −74.38 | 360 | 30 | 100 | 5.0 | Mw = 3.0 | SLU |
| Indiana | 2010 | 40.43 | −86.88 | 305 | 65 | 10 | 4.9 | Mw = 3.8 | SLU |
| Illinois | 2008 | 38.45 | −87.89 | 295 | 85 | 0 | 11.6 | Mw = 5.2 | SLU |
| Quebec, Canada | 2006 | 45.65 | −75.23 | 145 | 50 | 85 | 20 | Mw = 3.6 | SLU |
| Quebec, Canada | 2006 | 47.38 | −70.46 | 15 | 55 | 85 | 25 | Mw = 3.8 | SLU |
| Ohio | 2006 | 41.84 | −81.17 | 275 | 75 | 0 | 5 | Mw = 3.5 | SLU |
| Maine | 2006 | 47.0 | −68.79 | 170 | 25 | 45 | 5 | Mw = 3.5 | SLU |
| Quebec, Canada | 2005 | 47.75 | −69.73 | 170 | 60 | 80 | 18 | Mw = 4.6 | SLU |
| Tennessee | 2005 | 36.14 | −89.46 | 70 | 45 | 173 | 16 | Mw = 4.0 | SLU |
| Kentucky | 2005 | 36.95 | −89.0 | 320 | 80 | 15 | 4 | Mw = 3.6 | SLU |
| Ontario | 2005 | 44.68 | −80.48 | 320 | 25 | 65 | 11 | Mw = 3.6 | SLU |
| Missouri | 2004 | 36.73 | −89.68 | 27 | 40 | 116 | 4.5 | Mw = 3.5 | SLU |

a 1° × 1° finite element grid (Flesch et al., 2001). Computing the deviatoric stress field requires three steps, of which the first step involves calculating the GPE variations. We use the crustal thickness and density model Crust1.0 (http://igppweb.ucsd.edu/~gabi/rem.html) along with ETOPO1 topography and bathymetry data (Amante & Eakins, 2009) to compute GPE. We next calculate the deviatoric stresses arising from those GPE variations by solving the depth integrated (from a variable surface elevation to a reference depth of 100 km below the sea level) force-balance equations on a global grid with lateral viscosity variations, using the "thin sheet" approximation (Ghosh et al., 2006, 2009). Earlier studies have shown that integrating to depths shallower or deeper than 100 km does not substantially affect the GPE differences and hence the associated deviatoric stresses (Ghosh et al., 2009; Hirschberg et al., 2018; Jay et al., 2018; Klein et al., 2009). The second step involves calculating deviatoric stresses associated with horizontal tractions acting at a specific reference depth (base of depth integration, 100 km below sea level), which are obtained from a global mantle circulation model driven by tomography and history of subduction (Wen & Anderson, 1997), along with lateral viscosity variations in the lithosphere (Ghosh et al., 2008; Ghosh & Holt, 2012). It should be noted that the effects of the continental keels are embedded in the mantle circulation model (Ghost, Holt, & Wen, 2013). Both the GPE variations and tractions act as effective body forces in the force balance equations. The effective body force distribution provides the primary control on the magnitudes of deviatoric stresses acting within the lithosphere. The third step requires adding the GPE contribution to the contribution from horizontal basal tractions. As the force balance equations are linear in stress, it is possible to add the two separate contributions to obtain a total stress solution (Ghosh et al., 2008). Benchmarking shows that for a single-viscosity

**Table 1** *(continued)*

| Name | Year | Latitude | Longitude | Strike | Dip | Rake | Depth (km) | Magnitude | Reference |
|---|---|---|---|---|---|---|---|---|---|
| Illinois | 2004 | 41.44 | −88.96 | 20 | 90 | −165 | 5 | Mw = 4.5 | SLU |
| Kentucky | 2004 | 36.86 | −89.17 | 43 | 71 | 159 | 4 | Mw = 3.5 | SLU |
| New York | 2004 | 43.69 | −78.25 | 125 | 65 | 35 | 3 | Mw = 3.2 | SLU |
| Alabama | 2004 | 33.18 | −86.92 | 235 | 50 | −60 | 4 | Mw = 3.6 | SLU |
| Indiana | 2004 | 39.62 | −85.76 | 226 | 75 | 164 | 13 | Mw = 3.8 | SLU |
| Alabama | 2004 | 32.97 | −87.90 | 35 | 40 | −115 | 5 | Mw = 4.2 | SLU |
| Alabama | 2003 | 34.54 | −85.63 | 275 | 75 | 5 | 15 | Mw = 4.6 | SLU |
| Virginia | 2003 | 37.75 | −78.07 | 3 | 71 | 158 | 5 | Mw = 3.5 | SLU |
| S. Carolina | 2002 | −80.07 | 32.36 | 170 | 50 | 90 | 9 | Mw = 4 | SLU |
| Alabama | 1997 | −87.34 | 31.12 | 280 | 45 | −90 | 10 | Mw = 4.8 | SLU |
| Arkansas | 1996 | −90.0 | 35.97 | 120 | 65 | 15 | 5 | Mw = 3.8 | SLU |
| Quebec, Canada | 1975 | −76.22 | 46.46 | 162 | 49 | 118 | 15 | mb = 4.1 | Horner et al. (1978) |
| Delaware | 1973 | −75.41 | 39.72 | 26 | 11 | 90 | 6 | mb = 3.8 | Sbar et al. (1975) |
| Central Virginia | 1977 | −77.70 | 38.00 | 33 | 69 | 90 | 1 | mb = 1.5 | Yang and Aggarwal (1981) |
| Maine | 1979 | −69.80 | 43.98 | 190 | 54 | 90 | <5 | mb = 4 | Yang and Aggarwal (1981) |
| New York | 1966 | −78.20 | 42.80 | 13 | 71 | 159 | 2 | mb = 4.6 | Yang and Aggarwal (1981) |
| Maine | 1973 | −70.97 | 45.28 | 144 | 52 | 56 | 7 | mb = 4.8 | Yang and Aggarwal (1981) |
| New Jersey | 1977 | −74.77 | 40.80 | 32 | 53 | 77 | <1 | mb = 2.3 | Yang and Aggarwal (1981) |
| New Hampshire | 1977 | −71.65 | 43.19 | 4 | 45 | 49 | 0 | mb = 3.2 | Yang and Aggarwal (1981) |
| New Jersey | 1976 | −74.05 | 40.83 | 117 | 30 | 15 | 2.5 | mb = 3 | Yang and Aggarwal (1981) |
| New Jersey | 1976 | −74.35 | 40.95 | 11 | 7 | 71 | <2 | mb = 2.6 | Yang and Aggarwal (1981) |
| New York | 1976 | −73.76 | 41.13 | 38 | 80 | 119 | 5.3 | mb = 2.5 | Yang and Aggarwal (1981) |
| New York | 1976 | −73.86 | 40.99 | 1 | 66 | 64 | 5 | mb = 1.9 | Yang and Aggarwal (1981) |
| New York | 1977 | −74.15 | 41.18 | 215 | 72 | 103 | 6 | mb = 2.2 | Yang and Aggarwal (1981) |

lithosphere, it is possible to use the method described to recover the exact horizontal components of stress within a full 3-D model as long as the GPE and the basal lithosphere traction fields (associated with mantle convection) are known (Ghosh et al., 2008). In addition to lateral density variations (Naliboff et al., 2012), stresses are also dependent on the lateral variations in effective viscosity of the lithosphere (Naliboff et al., 2009) and, if relative variations are known, then it is possible to recover the exact stresses (Ghosh, Holt, & Wen, 2013; Klein et al., 2009). For all global calculations in this paper we use the optimal radial and lateral viscosity variations of the lithosphere and whole mantle defined by Ghosh, Holt, and Wen (2013), which was obtained by exhaustive testing of hundreds of possible viscosity models to isolate those models that satisfy constraints provided by plate motions, stress measurements, strain rates in plate boundary zones, and the geoid. For this present study, the relevant adjustments to the prior viscosity models of Ghosh, Holt, and Wen (2013) involve the exploration of lateral effective viscosity variations within the North American plate. This exploration of the influence of first-order effective viscosity variations within the North American plate enables us to place bounds on the minimum effective viscosity, as well as maximum and expected rates of long-term strain rate accommodated across the North American intraplate setting.

### 2.2. Absolute Viscosity, Strain Rates, and Velocity Field

Along with deviatoric stresses, the finite element model also produces relative values of velocities and strain rates. Although the orientation and magnitude of the deviatoric stresses are controlled by effective body forces and relative viscosity variations, the absolute values of velocities and strain rates depend on absolute values of the effective viscosities of the lithosphere. These absolute values are calculated by a postprocessing step that has no effect on the deviatoric stress solution. We place our global velocity field in a kinematic no-net-rotation (NNR) frame that involves finding the single rigid body rotation so that the entire global velocity field satisfies the NNR constraint. We then find the single scaling factor for the entire global viscosity field that minimizes the misfit between the dynamic (predicted) and the kinematic (constrained by GPS observations) velocity field (Kreemer et al., 2006) in an NNR frame. This single scaling factor determines the

**Table 1** *(continued)*

| Name | Year | Latitude | Longitude | Strike | Dip | Rake | Depth (km) | Magnitude | Reference |
|---|---|---|---|---|---|---|---|---|---|
| New York | 1975 | −73.95 | 41.14 | 186 | 27 | 90 | 3 | mb = 2.3 | Yang and Aggarwal (1981) |
| New Jersey | 1975 | −73.79 | 41.43 | 21 | 16 | 60 | 3 | mb = 2.3 | Yang and Aggarwal (1981) |
| New York | 1976 | −73.95 | 41.29 | 24 | 28 | 83 | 7.9 | mb = 1.8 | Yang and Aggarwal (1981) |
| New York | 1974 | −73.95 | 41.6 | 13 | 28 | 72 | 1.5 | mb = 3.3 | Yang and Aggarwal (1981) |
| Canada | 1978 | −74.37 | 45.64 | 134 | 53 | 102 | <5 | mb = 3.8 | Yang and Aggarwal (1981) |
| New York | 1978 | −74.51 | 44.52 | 159 | 72 | 108 | 1 | mb = 1.9 | Yang and Aggarwal (1981) |
| New York | 1971 | −74.45 | 43.81 | 161 | 27.5 | 91 | <5 | mb = 3.2 | Yang and Aggarwal (1981) |
| New York | 1975 | −74.64 | 43.91 | 160 | 39 | 91 | 3.7 | mb = 3.9 | Yang and Aggarwal (1981) |
| New York | 1976 | −74.63 | 44.58 | 160 | 38 | 89 | 1 | mb = 2.8 | Yang and Aggarwal (1981) |
| New York | 1975 | −73.57 | 44.89 | 163 | 38 | 90 | 13 | mb = 4.2 | Yang and Aggarwal (1981) |
| New York | 1975 | −74.55 | 44.89 | 179 | 29 | 104 | 0 | mb = 2.8 | Yang and Aggarwal (1981) |
| New York | 1974 | −74.03 | −45.04 | 152 | 41 | 80 | <5 | mb = 2.9 | Yang and Aggarwal (1981) |

*Note.* SLU stands for Saint Louis University Earthquake Center (http://www.eas.slu.edu/eqc/eqc_mt/MECH.NA/). CMT = Centroid-Moment-Tensor; NA = not available.

absolute values for the global viscosity field, strain rate field, and velocity field (Ghosh & Holt, 2012; Ghosh, Holt, & Wen, 2013).

Both radial and lateral viscosity variations are also incorporated into the model and have been constrained in the global model through the matching of strain tensor orientations in plate boundary zones, stress orientations in the plates and plate boundary zones, and plate motions. The methodology has been discussed in detail in Ghosh, Holt and Wen (2013). Although the global model of Ghosh and Holt (2012) showed "plate-like" behavior, the magnitudes of internal strain within the plates were nonzero and were governed by the absolute levels of effective viscosity for the plates, along with lateral variations within the plates. The details of internal lateral effective viscosity variations of the plates are unknown and may be controlled by the location of preexisting rift structures (Sykes, 1978), terrane boundaries and ancient orogenic fault zones (Hughes et al., 2015; Keller & Hatcher, 1999; Mooney et al., 2012), heat flow anomalies (Liu & Zoback, 1997), crustal anomalies (Kenner & Segall, 2000), and the state of mantle geotherm, composition, and water content (Burgmann & Dresen, 2008; Hirth, 2002; Jackson et al., 2008; Kohlstedt et al., 1995; Murphy & Egbert, 2017). We show that a simple first-order viscosity contrast (factor of 2) between juxtaposed strong continental craton, weaker Appalachian accreted terranes, and stronger ancient oceanic lithosphere of the west Atlantic block, when accounting for influences of topography, lithosphere structure, and coupling with mantle flow, provides a first-order match to the orientations of maximum shortening directions within the CEUS inferred from earthquake focal mechanisms.

### 2.3. Lateral Strength Variations

As proposed by Li et al. (2007) and Mooney et al. (2012), lateral variations in rheology can play a major role in the occurrence of intraplate seismicity. Here we test four primary models of lateral viscosity variations. The first one (Model 1) has lateral viscosity variations arising from weak plate boundaries (2–4 orders of magnitude weaker than intraplate areas) and a uniform lithosphere viscosity (Figure 1a). Model 2 is our best model from Ghosh, Holt, & Wen (2013) that gave an optimum fit globally to plate boundary deformation, intraplate stresses, and plate velocities. In addition to the weak zones, Model 2 consists of stiff cratons (an order of magnitude stronger than intraplate areas) as well as laterally variable oceanic lithosphere with areas older than 70 Ma having an effective viscosity the same as cratons and those younger than 70 Ma having a viscosity similar to the intraplate areas (Figure 1b). For the third model (Model 3), we have extended the eastern boundary of the North American craton farther to the east up to the ancient Laurentian margin, located along the position of the Appalachian gravity gradient (AGG; Figure 1c). The AGG is believed to be a structural boundary that marks the western limit of the thin crust that lies east of the Appalachian mountains (Cook & Oliver, 1981; Pratt et al., 1988). Seismic results show that the lithosphere is much thinner east of this boundary in comparison to cratonic lithosphere to the west of the boundary (Liu & Gao, 2018; Shen & Ritzwoller, 2016; Yuan & Romanowicz, 2010). Our premise is that the lithosphere that constitutes accreted Appalachian terranes (Keller & Hatcher, 1999; Williams & Hatcher, 1982) will have a lower effective

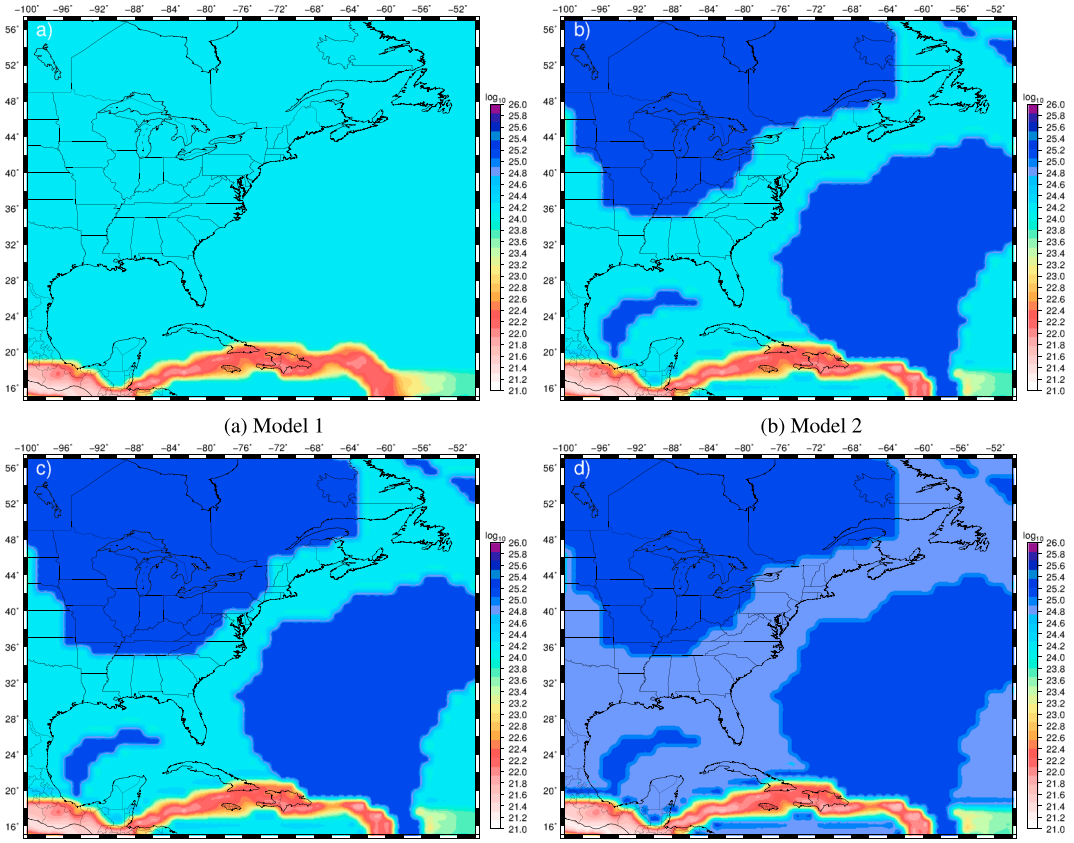


**Figure 1.** Actual "best fit" viscosity values that result from the fitting of kinematic plate motions from Kreemer et al. (2006; see section 2.2). (a) The entire North American plate has a single viscosity ($10^{24}$ Pa·s), while the lateral variations are only due to the presence of weak plate boundaries. (b) Addition of high viscosity keel and strong oceanic lithosphere ($> 10^{25}$ Pa·s) for areas older than 70 Ma. (c) The easternmost part of the high viscosity craton extends farther to the east up to the AGG, representing the location of the ancient Laurentian margin. The zone in between the two strong blocks is an order of magnitude weaker ($10^{24}$ Pa·s). (d) Same as in (b) except the area between the craton and the west Atlantic block has an intermediate viscosity value of $5 \times 10^{24}$ Pa·s.

viscosity in comparison with cratonic lithosphere to the west and old oceanic lithosphere to the east. In the fourth and final model, we modify Model 2, such that the weaker zone of accreted Appalachian terranes involves a viscosity contrast that is only a factor of 2 weaker than the continental craton and old oceanic regions (Model 4; Figure 1d). In other words, the accreted Appalachian terranes are treated the same as all normal continental lithosphere in the model, but this normal lithosphere is only a factor of 2 weaker than the cratonic lithosphere. For each of these viscosity models, we predict deviatoric stresses, strain rates and velocities.

## 3. Results

### 3.1. Strain Rates From GPS

We have investigated the Continuously Operating Reference Station (CORS) GPS data for North America to place bounds on the magnitudes of intraplate strain rates within eastern North America (Kreemer et al., 2014). We performed a damped least squares inversion of velocities to estimate a smoothed velocity gradient tensor field (spatial gradient estimates of a model velocity field; Haines & Holt, 1993; Holt et al., 2000; Figure 2b). We constructed a $1° \times 1°$ grid that covers CEUS, as well as regions within Canada. The solution constitutes the minimum magnitude of a strain rate associated with a continuous velocity field that matches the GPS data at their respective locations within a desired level of misfit. For our case, we seek a damping or smoothing such that the reduced chi-square misfit between observed and model velocities (within the defined reference frame provided by Kreemer et al., 2014) divided by the number of degrees of freedom is equal to 1.0. The solution in Figure 2b is similar to the strain rate solution recently published by

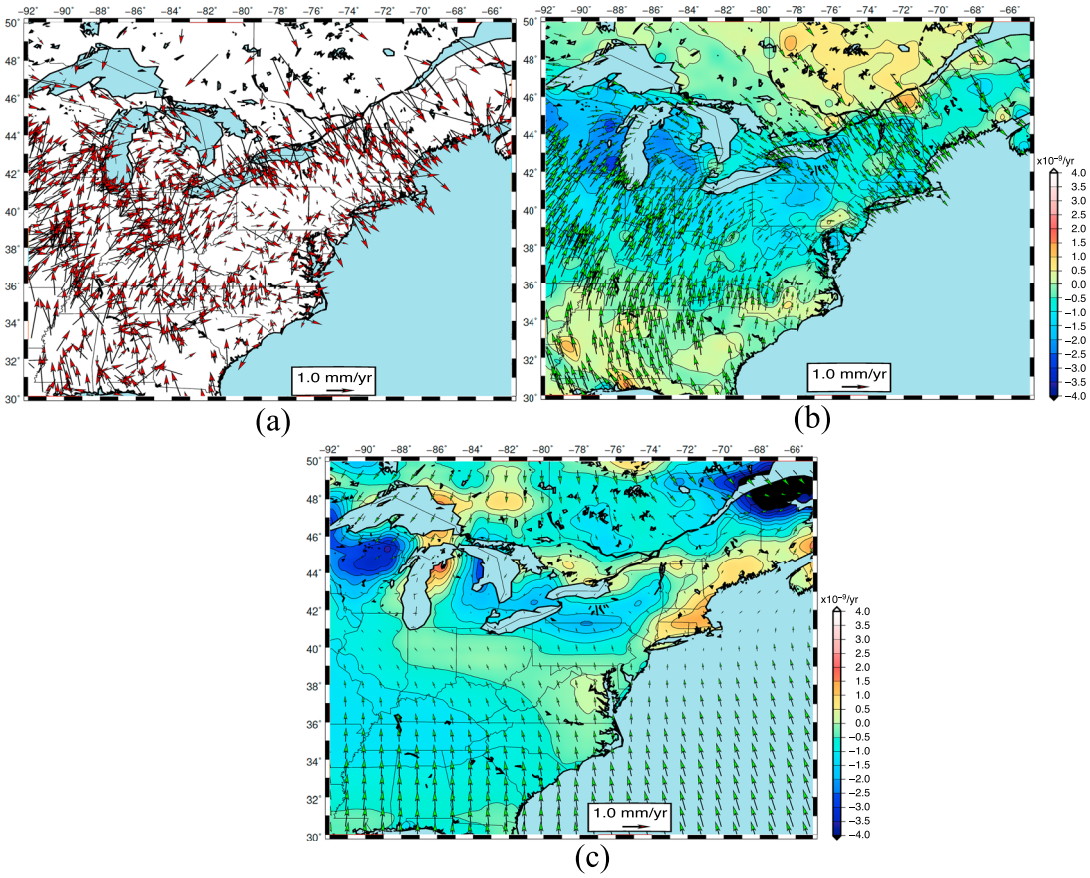


**Figure 2.** (a) Observed Continuously Operating Reference Station network velocities from Kreemer et al. (2014). (b) Model velocity field fit to observed GPS field obtained from damped least squares inversion (Beavan & Haines, 2001; Holt et al., 2000) with a reduced chi-square misfit between model velocity and observed GPS per degree of freedom of 0.98. The contoured values are dilatational strain rates from the smoothed model. (c) ICE-6G model (Argus et al., 2014; Peltier et al., 2015) velocity field with contoured dilatational strain rates.

Kreemer et al. (2018), and it shows a signal that can be interpreted to be dominated by GIA (Calais et al., 2006; Sella et al., 2007).

The model velocity field in Figure 2b provides a reduced chi-square misfit per degree of freedom of 0.98. Smaller values of reduced chi-square misfit per degree of freedom (resulting from overfitting the data) produce a strain rate field that contains high-amplitude strain anomalies in places where velocities show rapid spatial changes. We are after a solution that smooths through velocity outliers. The methodology provides an a posteriori variance-covariance matrix for model strain rates.

Using the horizontal velocities associated with the ICE-6G_C (VM5a) model (hereafter called just ICE-6G; Argus et al., 2014; Peltier et al., 2015), we have also computed exact solutions of the horizontal velocity gradient tensor field associated with this GIA model (Figure 2c). That is, no smoothing or damping is applied to the fitting of the GIA model velocities, as we are interested in the exact pattern of strain rates associated with the ICE-6G model. Comparison of the ICE-6G model with the GPS model shows significant overall similarities between the two fields: both solutions show a northward motion in regions south of ~40°N of about 1 mm/year and both solutions show a belt of contractional dilatational strain rates through the Great Lakes region and into Northeast Canada (Figures 2b and 2c). Strain rate magntiudes from the GPS model are slightly higher than the ICE-6G model in some regions and show dilatation rates of $\pm 2\text{–}3 \times 10^{-9}$ year$^{-1}$. There are also substantial differences between the dilatational strain rate patterns and velocity fields for the two solutions.

Strain rates are independent of reference frame definition, and we compare the principal axes of strain rates from ICE-6G model with that obtained from the smoothed interpolation of the CORS GPS data (Figures 3a and 3b). Contraction rates are generally radially directed away from the paleo-ice load, consistent with the

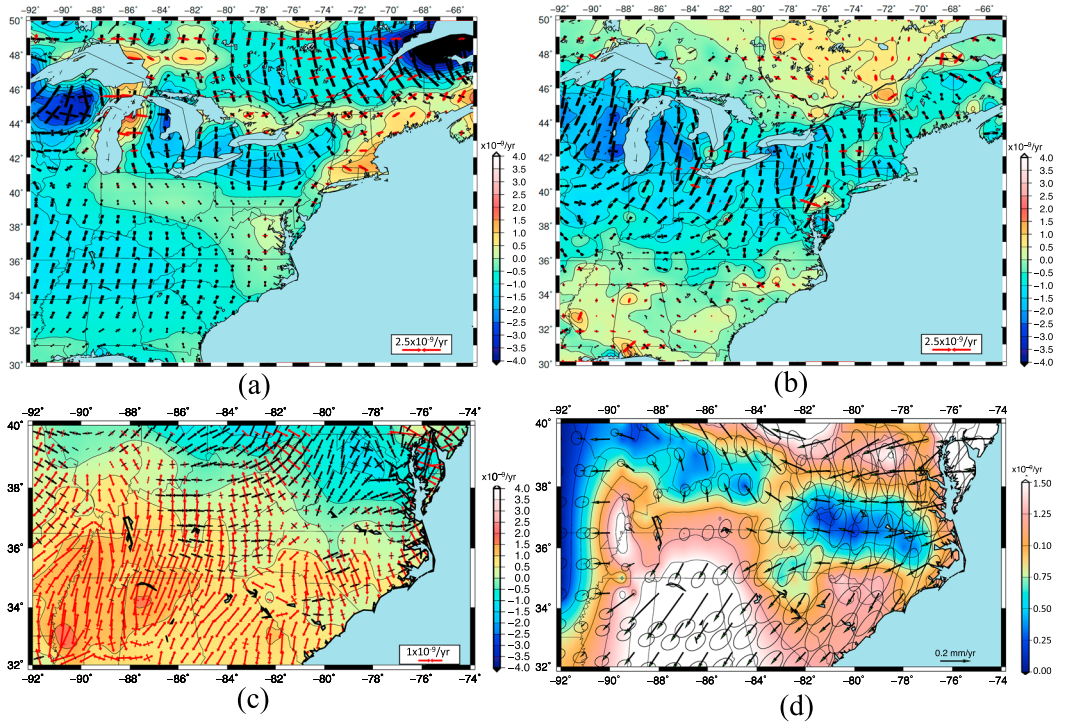


**Figure 3.** (a) Principal axes of strain rates (black are compressional, red are extensional) from the ICE-6G model, plotted on top of contoured dilatational strain rates. (b) Principal axes of strain rates from solution in Figure 2b, plotted on top of contoured dilatational strain rates. (c) Residual strain rate field (principal axes of strain rates plotted on top of dilatation rates) resulting by the subtraction of the ICE-6G model (model GIA effects) from the GPS model. The residual strain rate field plotted contains a potential tectonic signal, plus errors in GPS measurements and errors in the GIA model. This residual model shows a total amount of shortening between New Madrid and coastal Virginia of 0.45 ± 0.25 mm/year in a ENE-WSW direction. (d) Velocity field relative to central United States region associated with the residual strain rate field in (c). Error ellipses are for 1 sigma. GIA = glacial isostatic adjustment.

GIA-dominated signal (Figure 3a). However, the CORS GPS solution (Figure 3b) shows significant differences from the ICE-6G model. There are three fundamental differences between the two strain rate fields: (1) radial compression rates are present further north in ICE-6G solution (within southern Canada) that are not present in the CORS GPS solution; (2) there are roughly N-S oriented contractional strain rates in the south (between 32°N and 40°N) in the ICE-6G model that are not observed in the CORS GPS solution; and (3) the CORS GPS solution (Figure 3b) shows the presence of a component of ENE-WSW contraction (across Kentucky, Tennessee, parts of eastern Virginia) that the ICE-6G solution model does not possess (Figures 3a and 3b). Because the GIA signal is strong in the north (near the paleo-ice load), we focus our analysis south of 40°N. Comparison of the ice load response with the GPS horizontal field of velocities and strain rates (Figures 2b, 3a, and 3b) indicates that the strain rate field is dominated by GIA processes (Calais et al., 2006; Kreemer et al., 2018; Sella et al., 2007). We will show later that the principal axes of shortening from the GIA component of the signal are generally orthogonal to the observed $SH_{max}$ directions of stress obtained from focal mechanism inversion and generally orthogonal to maximum shortening directions shown with earthquake *P* axes.

A tectonic signal, if detectable, would be embedded in the total strain rate field represented by the GPS observations (Figures 2a and 2b). To recover this tectonic signal, we subtract out the ICE-6G model strain rates (Figure 3a) from the CORS GPS strain rate solution (Figures 3b). Ignoring errors in the interpolated field of strain rates (Figures 2b and 3b) obtained from GPS, the residual strain rate field (Figure 3c) will be associated with either errors in the GIA model, a tectonic signal, or some combination of both. The residual strain rate field (Figure 3c) shows significant amounts of extensional strain rate south of 36.5°N and west of 80°W that is oriented in a roughly N-S direction. This extension in Figure 3c appears to be associated with the radial compression that is present in the ICE-6G model (Figure 3a) but that is not found in the CORS GPS solution (Figure 3b); subtraction of the ICE-6G model from the GPS solution thus gives the

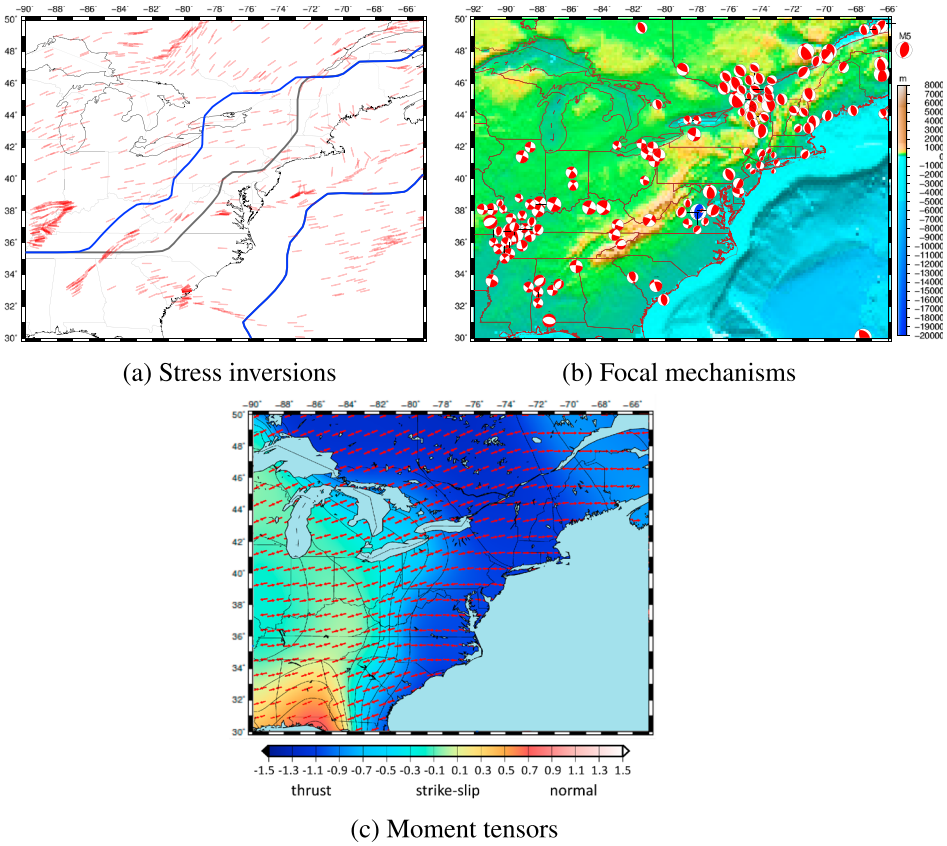


**Figure 4.** (a) $\sigma_{H\,\max}$ from stress inversions of Levandowski et al. (2018). Blue lines mark the eastern margin of the craton and the western margin of the strong west Atlantic block, whereas the gray line delineates the Appalachian gravity gradient boundary. (b) Focal mechanisms of eastern U.S. earthquakes compiled from various sources (see Table 1) plotted on topography. The focal mechanism of the Virginia quake is shown in blue. (c) Directions of maximum shortening (red principal axes) obtained by applying a smoothing filter to uniformly weighted moment tensors of all events in (b). The color contours represent the ratio of the sum of principal axes, normalized by the magnitude of principal axes; this ratio represents focal mechanism style of the smoothed tensor field. Coastal regions are dominated by thrust style, whereas regions west of the Appalachians and southwest of the Great Lakes are dominated by strike-slip regime.

roughly N-S extension within these regions in the south within the residual model (Figure 3c). Because these principal axes of extension are radially oriented toward the paleo-ice load (roughly N-S), we interpret such differences as possible errors in the GIA model. However, a feature of interest within the residual field of Figure 3c, which may not be due to errors in GIA modeling, consists of compressional strain rates that have principal axes oriented in a ENE-WSW direction within Kentucky, Tennessee, parts of West Virginia, Virginia, and North and South Carolina. These hold interest because they are the expected direction of shortening and stress based on the focal mechanism data (Figure 4; Levandowski et al., 2018). Because the ENE-WSW orientations of contractional strain rate in Figure 3c are unlike any GIA signal (dominated by radial contractional strain in a roughly N-S direction), we interpret this component of the residual strain rate as a potential long-term tectonic signal. Relative to a fixed frame located at 90°W, these residual strain rates accommodate up to 0.45 ±0.25 mm/year (1-sigma error) of ENE-WSW contraction between 88°W and 76°W longitudes (Figure 3d). The average contractional strain rate is $\sim 0.5 \times 10^{-9}$ year$^{-1}$ across this zone (Figure 3c). Residual strain rates in eastern Tennessee are strike slip in style, whereas across parts of Virginia the contractional strain rates are generally thrust style (Figure 3c). Residual strain rates south of about 38°N, where we have more confidence that the GIA signal is expected to be smaller (Figure 3a), are generally less than $1 \times 10^{-9}$ year$^{-1}$ (Figure 3c). Therefore, a strain rate of $1 \times 10^{-9}$ year$^{-1}$ is considered an upper bound constraint on the magnitudes of expected long-term strain rate associated with tectonic processes. This upper bound on strain rate magnitudes of $1 \times 10^{-9}$ year$^{-1}$ is an important constraint in the dynamic models. That is, the body forces (GPE differences and influences of coupling with mantle flow) place bounds on the stress

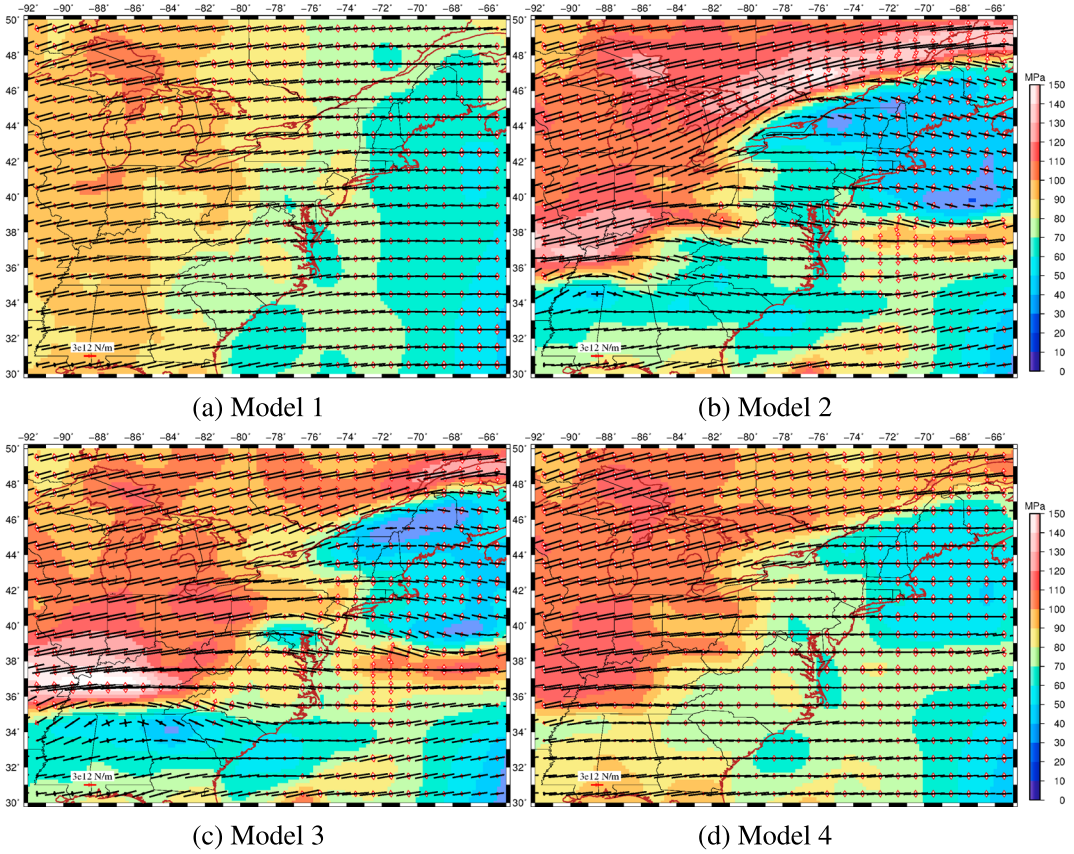


**Figure 5.** Predicted deviatoric stresses from the (a–d) four viscosity models in Figure 1 plotted on top of their second invariants. Black arrows indicate compression, whereas red indicate tensional stresses.

magnitudes within the plates. Having an upper bound on expected strain rate magnitudes will enable us to investigate first-order strength variations within the plates (craton vs. accreted Appalachian terranes) and provide a lower bound on effective viscosity for these regions. That is, we will reject lithosphere viscosity models that predict strain rates higher than $1 \times 10^{-9}$ year$^{-1}$ over relatively broad regions. Moreover, the geodetic constraints on strain rates, and the dynamic solutions that satisfy these constraints, provide the basis for important statistical measures of long-term expected seismic hazards estimates (Bird et al., 2010; Bird & Liu, 2007; Kagan & Jackson, 1994).

### 3.2. Deviatoric Stress Predictions

The *P* axes or the maximum shortening directions of earthquake focal mechanisms approximately follow the directions of the regional $SH_{max}$, which is the most compressive horizontal principal axis. However, these maximum stress directions may deviate from *P* axes of earthquakes in cases where there is no fresh rupture and especially in the case of shallow earthquakes (McKenzie, 1969). Mazzotti and Townend (2010) showed that there is as much as a 30–50° rotation of *P* axes for the earthquakes in the central Virginia seismic zone relative to the regional $SH_{max}$ direction. Here we use the maximum compressive stress directions ($\sigma_{H\,max}$) determined from spatially weighted inversions of focal mechanisms by Levandowski et al. (2018; Figure 4a). We apply a smoothing technique to the stress inversions from Levandowski et al. (2018) in order to remap them on our 1° × 1° grid. The general trend of the inverted stress is NE-SW; however, there is a slight change in orientation with changing latitudes. The trend is more ENE-WSW (~60–90°) between 39° and 46° latitude, while north and south of that region, the orientation is NE (40–60°). We also use the *P* axes of individual focal mechanisms as constraints (Figure 4b), which are compiled from various sources (see Table 1). The focal mechanisms represent permanent strain events. The patterns of strain (orientations of shortening axes and style of strain) can be compared with orientations of strain obtained from the dynamic model. Our assumption in the dynamic model is that there is an isotropic relationship between stress and strain rate. Although this is an oversimplification, our premise is that a sum of normalized moment ten-

sors within a given region will reflect the average state of strain orientation that can be compared with the dynamic model. We perform a Kostrov moment tensor summation, where each event is normalized so that the moment tensors from each event are of equal weight. The size of the areas for the moment tensor summation is 1° × 1°. We then spatially smooth the moment tensor field (Figure 4c). We compare the tensor orientations from the smoothed seismic moment tensor field with the predictions of stress tensors from the dynamic model by computing a correlation function.

The combined deviatoric stress field from a uniformly strong North American plate model (Model 1) shows nearly uniform ENE-WSW directed compressional stresses (Figure 5a). The dominant stress pattern in eastern North America is primarily NE-SW directed compressional stresses, as has been shown earlier by Zoback and Zoback (1981) and more recently by Levandowski et al. (2018). The effect of sandwiching a region with lower effective viscosity (accreted Appalachian terranes), which lies between the craton and the old oceanic lithosphere (Model 2), is to reorient the maximum principal stress axes along most of the eastern seaboard to WNW-ESE (270–290°), which is rotated toward the normal to the strike of the boundaries of the viscosity contrasts (Figure 5b). West of the viscosity contrast, within the stronger cratonic regions, maximum principal stress orientations remain in the NE-SW direction (60–70°). This reorientation of principal stress directions has the effect of an improvement in the fitting of the strain orientations associated with some earthquakes along the eastern seaboard, including the Virginia quake, where the dominant mechanism involves WNW-ESE contraction associated with primarily thrust faulting (Figure 4b). The largest stresses occur within parts of the cratonic region, including the area around New Madrid. Model 3 moves the location of the transition in orientation of the maximum principal stress axes (from WNW-ESE to NE-SW) farther to the east (Figure 5c) and yields a slightly improved fit to the *P* axis of the Virginia quake (Figure 5c). However, it should be noted that the Central Virginia Seismic Zone is complex and there occurs a difference in the orientation of the seismically inferred maximum compressive stress and that determined from boreholes as shown by Mazzotti and Townend (2010) and Kim and Chapman (2005). The stress inversions from Levandowski et al. (2018) show an E-W orientation of maximum principal stress in the Central Virginia Seismic Zone (Figure 4a), which is close to our model predictions of roughly E-W shortening in Models 1 and 4 for this region (Figures 5a and 5d). A prominent high stress concentration is observed in the vicinity of the New Madrid region, an observation similar to Levandowski et al. (2016), which he ascribed as owing to the presence of a dense lower crust. The higher stresses for Model 3 result from a stress guide effect associated with both the geometry of the high viscosity cratonic lithosphere and the viscosity contrast adjacent to the weaker zone of Appalachian terranes. A slightly stronger zone of Appalachian terrane lithosphere (Model 4), where the reduction in effective viscosity is only a factor of 2 lower than that of the craton, makes the maximum principal shortening directions along the eastern seaboard region in a roughly E-W direction (Figure 5d), similar to that obtained in Model 1 with a single intraplate viscosity. The transition from roughly E-W maximum shortening along the eastern seaboard to NE-SW oriented maximum shortening within the continental interior occurs more gradually in Models 1 and 4 in comparison with the sharper transition that occurs for Models 2 and 3.

### 3.3. Comparison With Earthquake *P* Axes, Moment Tensors, and Stress Indicators

The predicted deviatoric stress field in general provides a first-order match to the *P* axes of the focal mechanisms within central and eastern North America (Figure 6). An average angular misfit of ~22° is found for the case with a single intraplate viscosity. With the exception of a few events with NE-SW oriented shortening directions in South Carolina, focal mechanisms east of the AGG (eastern seaboard) show a dominantly thrust pattern, with the *P* axes typically oriented WNW-ESE (270–290°; Figures 4b and 4c). The WNW-ESE oriented *P* axes for such events are matched slightly better by the model orientation of maximum shortening when we allow for a strength contrast between the zone of weaker accreted Appalachian terranes and the stronger interior craton or Laurentian margin (Models 2 and 3). However, such a WNW-ESE orientation of predicted maximum shortening degrades the fit considerably to a few events in South Carolina (Figures 6b and 6c). For Model 2, in particular, the overall misfit is larger (~23°), whereas for Model 3 the overall misfit is slightly better than Models 1 and 2. The influence of the strength contrast is to produce a rotation in the principal axes of maximum compressional stress from WNW-ESE directions in the coastal regions to SW-NE directed within regions west of the strength contrast. This transition in orientation of inferred $SH_{max}$ stress directions was first noted by Zoback and Zoback (1980) and Zoback and Zoback (1981). Placing the strength

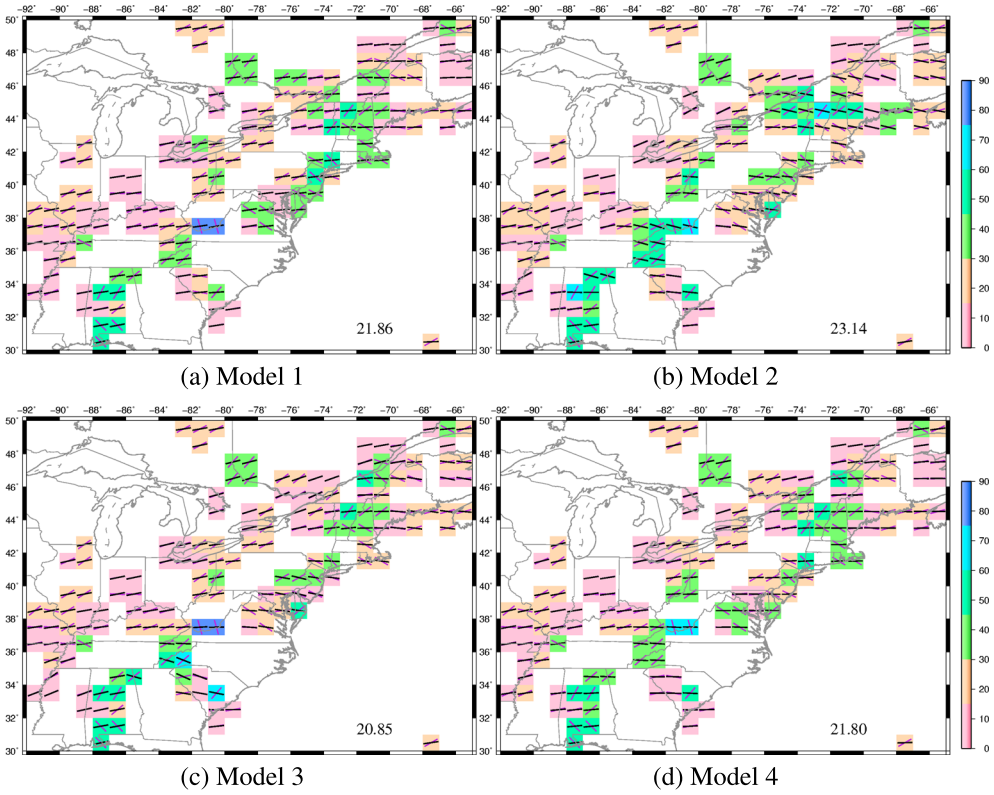


**Figure 6.** Angular deviation (a–d) between predicted maximum compressional direction (black bars) from various viscosity models and *P* axes of earthquakes (pink bars) compiled from various sources (see Table 1). The average deviation is noted on bottom right.

contrast at the craton boundary (Li et al., 2007; Model 2) produces this transition in stress orientation that appears to be too far west, inconsistent with the general transition in orientation of maximum shortening directions inferred from focal mechanisms (Figure 4), which yields a higher overall misfit to *P* axes in comparison with Model 3 (Figure 6). For Model 1, the North American plate is of one constant strength, and the maximum horizontal compressive stress axes show a gradual rotation from E-W along coastal regions (80–90°) to NE-SW within the craton interior (70–80°).

Mooney et al. (2012) hypothesized that the primary strength contrast in North America lies between the Archean and post-Proterozoic terranes (edge of craton). It remains of major importance to determine the magnitude of this strength contrast, along with its implications for the stress and strain rate field. We also experimented with a model that had a strong Archean craton and a gradational weakening into weakest accreted Appalachian terranes (Figure 1d). This model (Model 4) produced results (Figure 6d) similar to that of the single plate model (Model 1). The location of the AGG as a major lithospheric strength contrast, appears to provide a slightly better fit to the spatial transition in orientation of *P* axes (~21°; Figure 6c), although the differences in angular misfit between models is very small.

We next compare the modeled stresses with the smoothed stress indicators from Levandowski et al. (2018). Except for a few events in Maine, the predicted compression directions match the orientations of their $\sigma_{H\,\max}$ relatively closely (within ~20°) within the continental United States. Introduction of an order of magnitude strength contrast (Models 2 and 3) worsens the fit for a few inversions in eastern Tennessee, western North Carolina, and western Virginia (Figures 7b and 7c). Again, the differences in angular deviation for the four viscosity models is minimal (a variation of only 2°), with Model 4 yielding the lowest misfit (Figure 7d).

The comparison with earthquake moment tensors enables us to quantitatively evaluate the predicted deviatoric stress tensors in terms of both direction of principal axes as well as style of faulting. The correlation coefficient between normalized seismic moment tensors (Figure 4c) and deviatoric stress tensors from the

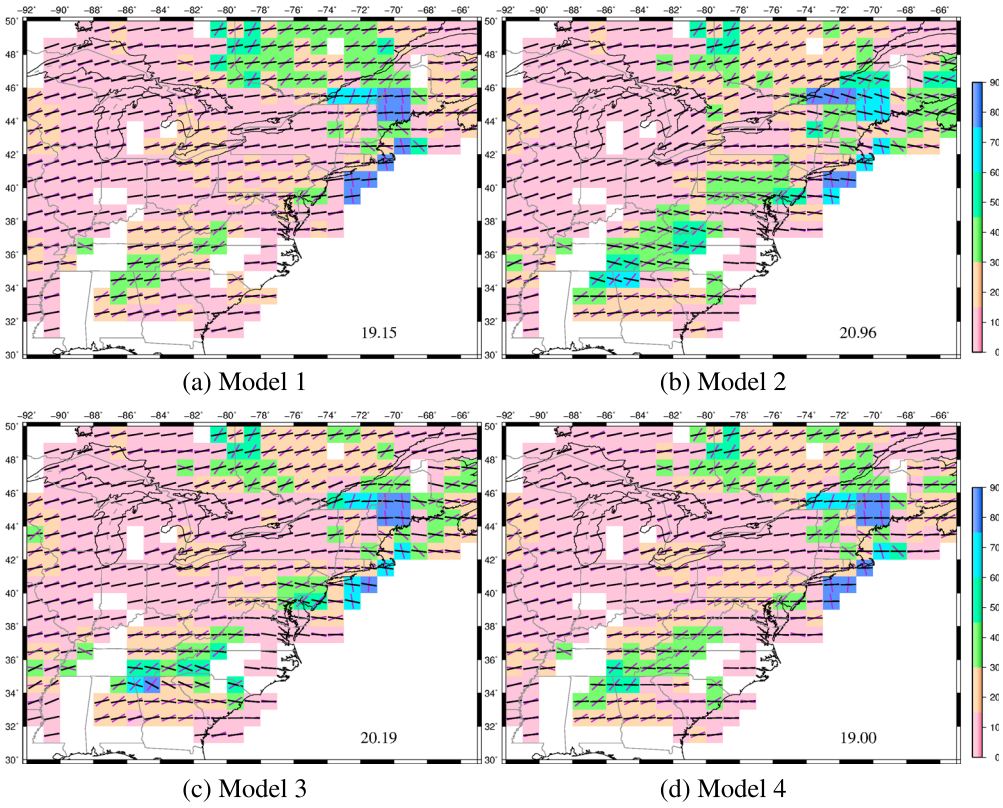


(a) Model 1 (b) Model 2

(c) Model 3 (d) Model 4

**Figure 7.** Angular deviation (a–d) between predicted maximum compressional direction (black bars) from various viscosity models and smoothed stress inversions from Levandowski et al. (2018; pink bars). The average deviation is noted on bottom right.

dynamic model (Figure 5) is defined as

$$-1 \le \sum_{\text{areas}} (\epsilon \cdot \tau)\Delta S / \left( \sqrt{\sum_{\text{areas}} (E^2)\Delta S} * \sqrt{\sum (T^2)\Delta S} \right) \le 1$$

(Ghosh et al., 2008), where $E = \sqrt{\epsilon_{\phi\phi}^2 + \epsilon_{\theta\theta}^2 + \epsilon_{rr}^2 + \epsilon_{\phi\theta}^2 + \epsilon_{\theta\phi}^2} = \sqrt{2\epsilon_{\phi\phi}^2 + 2\epsilon_{\phi\phi}\epsilon_{\theta\theta} + 2\epsilon_{\theta\theta}^2 + 2\epsilon_{\phi\theta}^2}$, $T = \sqrt{\tau_{\phi\phi}^2 + \tau_{\theta\theta}^2 + \tau_{rr}^2 + \tau_{\phi\theta}^2 + \tau_{\theta\phi}^2} = \sqrt{2\tau_{\phi\phi}^2 + 2\tau_{\phi\phi}\tau_{\theta\theta} + 2\tau_{\theta\theta}^2 + 2\tau_{\phi\theta}^2}$, and $\epsilon \cdot \tau = 2\epsilon_{\phi\phi}\tau_{\phi\phi} + \epsilon_{\phi\phi}\tau_{\theta\theta} + \epsilon_{\theta\theta}\tau_{\phi\phi} + 2\epsilon_{\theta\theta}\tau_{\theta\theta} + 2\epsilon_{\phi\theta}\tau_{\phi\theta}$. $E$ and $T$ are the second invariants of normalized seismic moment tensors and stress, respectively, $\epsilon_{ij}$ are the components of the seismic moment tensors compiled from various sources (Table 1), $\tau_{ij}$ are the components of the predicted deviatoric stresses from the dynamic models, and $\Delta S$ is the grid area. Normalization ensures that the correlation depends only on the directions and relative magnitudes of the principal axes of both deviatoric stress and moment tensors, and it removes dependence on magnitude of both stress and moment tensors. Although we have computed a smoothed field of the normalized moment tensors (Figure 4c), the correlation results shown in Figure 8 involve only the areas that contain events in Figure 4b. Viscosity Models 1, 3, and 4 yield good correlations with Model 1 giving the highest correlation (0.78; Figure 8). Viscosity Model 2, on the other hand, gives a correlation of less than 0.7. The degradation of fit is most likely due to the misfit to mechanisms in western North Carolina and eastern Tennessee, similar to that in Figure 6b.

Except for a few cases, the combined effects of GPE gradients and coupling with large-scale mantle flow predict deviatoric stress fields that match with the $P$ axes, $\sigma_{H\,\max}$, and the moment tensors derived from the earthquakes in CEUS. We have shown earlier that the geodetically constrained strain rate field is dominated by a GIA signal that possesses principal axes of shortening that are, for nearly all cases, roughly orthogonal to the maximum shortening directions obtained from $P$ axes of earthquakes as well as orthogonal to the directions of $\sigma_{H\,\max}$ from stress inversions. The above analysis then indicates that these earthquakes are the

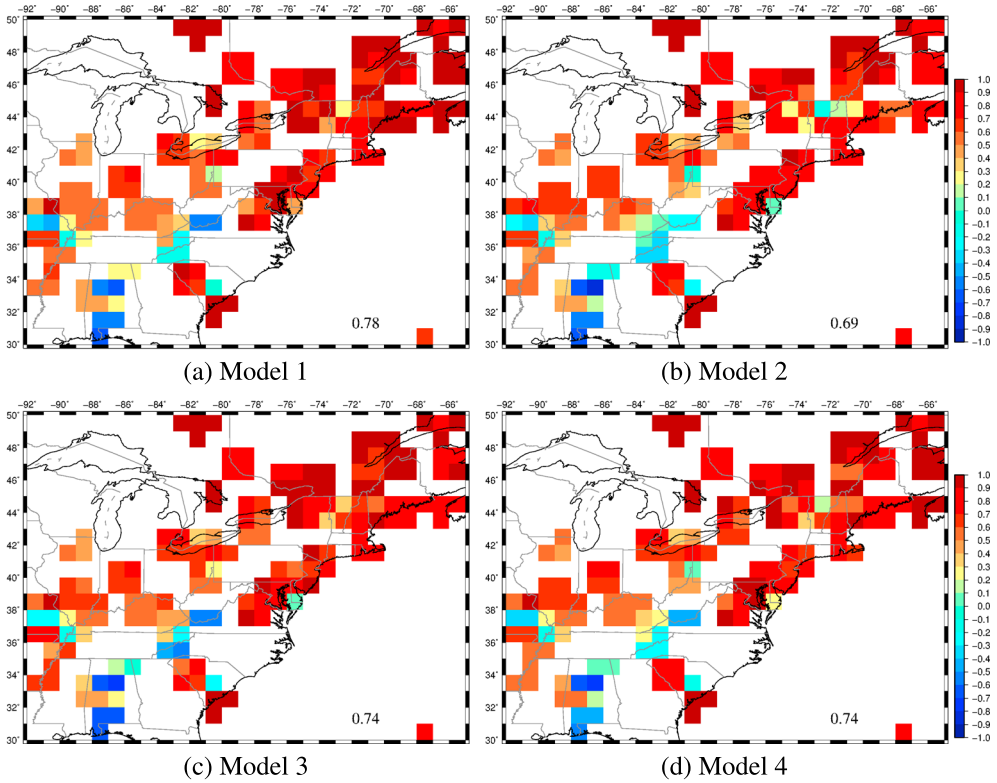


**Figure 8.** Correlation coefficients (a–d) between predicted deviatoric stress tensors from four different viscosity models and the earthquake moment tensors. The average correlation is noted on bottom right.

result of tectonic stresses, generated by the combination of the influence of topography and lithospheric structure, together with coupling with large-scale mantle flow. Although the four viscosity models generate stress fields that have slightly different orientations based on where we put the strength contrasts (Figure 5), the analyses of the misfits to the observations of stress orientations, P-axes, and the correlation with unit tensors of earthquakes is largely inconclusive, with the best models performing only slightly better than the worst. For example, Model 4, with a moderately strong lithosphere, sandwiched between a strong craton and a strong old oceanic lithosphere (Figure 1d), provides the smallest misfit (Figure 7) when compared to smoothed stress inversions from Levandowski et al. (2018). However, when we compare the predicted compressional stress axes with the actual *P* axes of the earthquakes, viscosity Model 3, with the AGG acting as a major lithospheric strength contrast provides the lowest misfit (Figure 6). A quantitative comparison with the seismic moment tensors yields a slightly better correlation for the case with a single intraplate viscosity (Figure 8). Hence, when comparing only model stress orientations with earthquake observations, it is not possible to draw a conclusion as to which of the viscosity structures is preferred when it comes to explaining the seismicity of eastern North America. Instead, we show here that accounting for both mantle convection and lithosphere structure and topography provides a first-order prediction for the stresses that match the earthquake stress and strain indicators to a large extent and, hence, could be responsible for the observed seismicity in CEUS. We next show that by introducing constraints on the expected upper bound of the magnitude of strain rates, using GPS observations, it is possible to constrain a lower bound for the effective viscosity for the craton, Appalachian terranes, and oceanic lithosphere. Such a model then predicts an upper bound for expected long-term seismic moment rates and strain rates across the margin of Eastern North America.

### 3.4. Prediction of Strain Rates and Velocities

The above results, which quantify depth integrated deviatoric stress magnitudes, have important implications about long-term strain rates of the lithosphere in this intraplate setting and associated seismic hazards. The prediction of strain rates and surface motions depends on the absolute values of effective viscosities of the lithosphere (craton, Appalachian terranes, and oceanic west Atlantic block). Assuming a constant

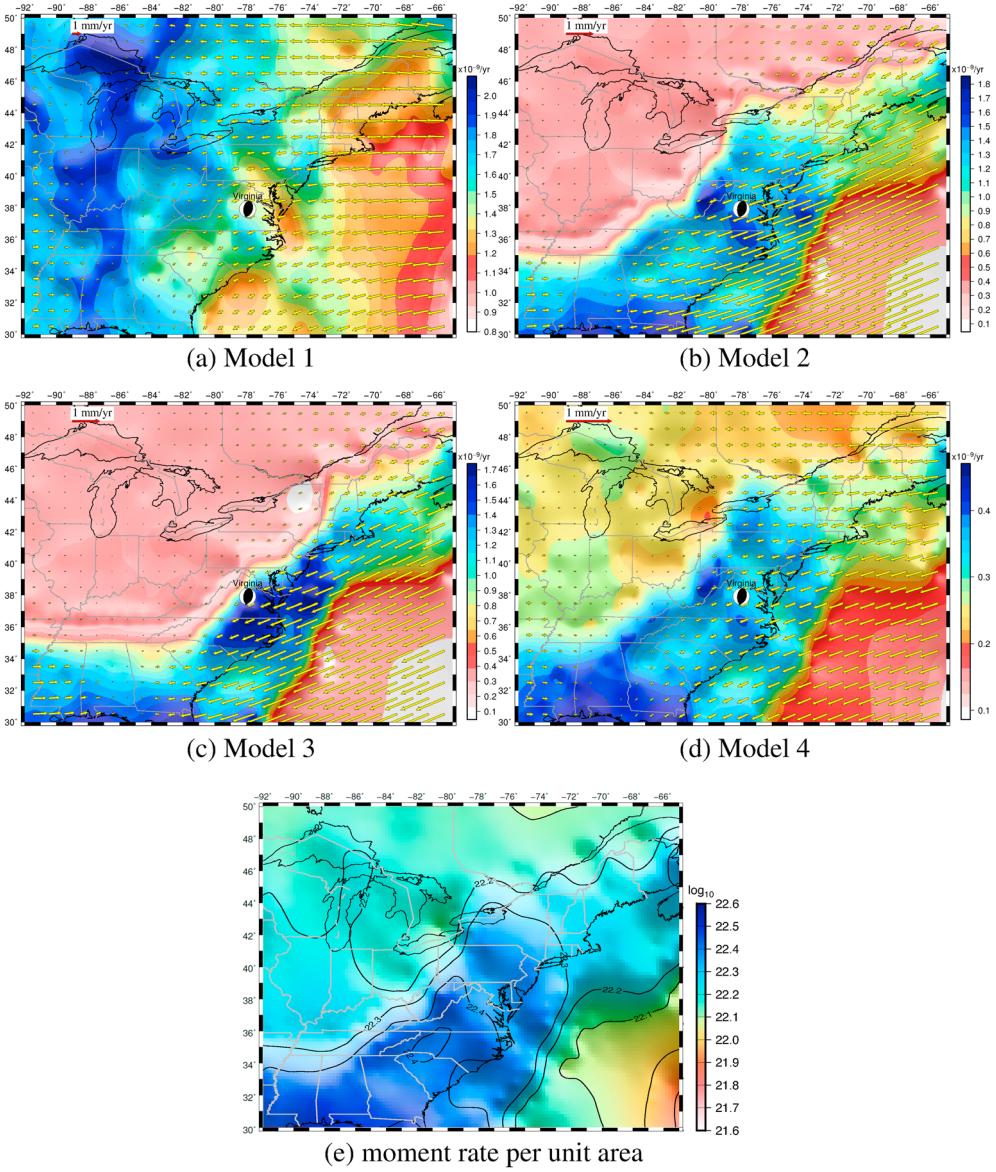


**Figure 9.** (a–d) Relative velocities accommodated across the zone of intraplate deformation (yellow vectors) plotted on top of modeled strain rates (second invariants) for the four different viscosity structures. The velocities are calculated with respect to North American lithosphere located within the Great Lakes region. The focal mechanism of the 2011 Mineral, Virginia, earthquake is also shown. Note change in velocity scale for the four solutions. (e) Contoured tectonic moment rates in dyne-cm/year per 1° × 1° areas, obtained from the strain rates in optimal Model 4, assuming a 15-km-thick seismogenic layer and a shear modulus of $3.0 \times 10^{10}$ N/m$^2$.

viscosity of ~$10^{24}$ Pa·s in the intraplate region (Model 1) yields deformation rates of ~1.5–2 × $10^{-9}$ year$^{-1}$ within the plate interior (Figure 9a). These deformation rates yield expected long-term contraction rates that accommodate more than 2-3 mm/year of relative motion between the longitudes of 90°W and 70°W. These rates greatly exceed the upper bound for expected contraction rates constrained using GPS and GIA model information (section 3.1). Assuming a viscosity value of ~$10^{25}$ Pa·s (Models 2 and 3) yields long-term horizontal strain rates of <3 × $10^{-10}$ year$^{-1}$ in the craton interior and within the west Atlantic oceanic block (Figures 9b and 9c). An effective viscosity contrast involving the lithosphere of accreted Appalachian terranes, results in long-term strain rates of 1.2–1.8 × $10^{-9}$ year$^{-1}$ and a total motion of ~0.25–0.75 mm/year across both the Piedmont and Coastal plain regions in the south, and across New England in the northeast United States (Figure 9b), which is likely an upper bound. Whereas stress magnitudes are a function of input body forces (coupling with mantle convection, and lithosphere topography and structure, Ghosh

& Holt, 2012), the strain rates are strongly dependent on the absolute viscosity of the lithosphere. For this model, there occurs a focusing of strain rate magnitudes in the region of Virginia and adjacent Coastal plain regions, as well as higher strain rates that overlap with the Eastern Tennessee seismic zone. Motions accommodated across the weaker internal boundary zone are in a southwest direction relative to interior North America (Figure 9b). The model also predicts significant strain rates offshore, owing to the assumption of the strength contrast located as far east as the transition between continental and oceanic lithosphere. Strains are partitioned, with shortening oriented more normal to the trend of the strength contrast between craton boundary and Appalachian terrane interior (such as the orientation of the thrust mechanism for the Mineral, Virginia, earthquake), whereas a greater component of strike-slip motion is accommodated offshore (Figure 5b). Interestingly, the Virginia earthquake sits within the zone of the highest strain rates for Model 2. However, the strain rates in Model 2 within the coastal regions of $1–2 \times 10^{-9}$ year$^{-1}$ still exceed the upper bound of long-term strain rates that were inferred in section 3.1. An order of magnitude strength contrast across the craton boundary apparently yields expected long-term strain rates that are too high. Model 3, with the strength contrast at the AGG boundary yields a strain rate high that covers the region from South Carolina to New Jersey and that peaks in magnitude within Virginia. The strain rate high is further to the east than in Model 2. The strain rate highs in areas of the Eastern Tennessee seismic zone are absent in Model 3. Furthermore, strain rate magnitudes of $\sim 2 \times 10^{-9}$ year$^{-1}$ for Model 3 exceed expected values from the GPS-constrained model. Model 4 is the same as Model 2, except that there is only a factor of 2 lower viscosity within the Appalachian terrane regions east of the craton and west of the old oceanic lithosphere. As such, Model 4 yields a strain rate pattern similar to Model 2, except that strain rate magnitudes are in the range of $3–5 \times 10^{-10}$ year$^{-}1$, which are at or below the acceptable maximum bound on long-term strain rates inferred from the model constrained by GPS (compare Figures 3c and 3d with Figure 9d). The magnitude of the southwest directed motions accommodated across the weaker Appalachian terrane is 0.25–0.35 mm/year, which is in rough agreement with the residual GPS field (Figure 3d). Within regions well south of the GIA-related zone of radial contractions (south of 38°N) the model predicts strain rates that are compatible with the residual strain rate field, obtained by subtracting the GIA model from the GPS model (Figure 3c). Given that Model 4 provides the acceptable range of strain rates, it is the preferred model. This southwest motion relative to the midwest interior of North America is a feature of all models and directions of relative velocities are largely controlled by the large-scale intraplate stress pattern (NE-SW) throughout the North American plate.

We argue that the GPS measured strain rates represent an elastic response within the upper portion of the lithosphere to stress rates. These stress rates are associated with two processes: (1) slow strain rates (typically less than $10^{-9}$ year$^{-1}$) associated with long-term tectonic loading (GPE gradients + mantle flow) and (2) transient GIA strain rates that produce shortening directions in the CEUS that are generally orthogonal to the long-term maximum compressive deviatoric stress directions. Motions measured to date using GPS show a GIA-dominated signal in north central and northeastern North America (Calais et al., 2006; Kreemer et al., 2018; Sella et al., 2007). Strain rates from this signal have principal axes directed radially outward from the ice sheet, which fit neither with most of the orientations of $P$ axes of focal mechanisms nor with the $\sigma_{H\,\mathrm{max}}$ directions from stress inversions (Figure 4). Furthermore, the influence of GIA diminishes exponentially away from the margin of the ice sheet and hence the role of GIA in affecting areas south of the hinge line is thought to be minimal (Wu & Johnston, 2000; Zoback, 1992). Using GPS to confirm shortening rates predicted by the tectonic effects described here will take many years to sufficiently resolve with higher precision, though the results we present here by subtracting out the GIA model show some possible evidence of NE-SW directed contraction between western Tennessee and Coastal Virginia that accommodates as much as $0.45 \pm 0.25$ mm/year of contraction related motion across this zone (Figure 3d). North of about 38°N the residual field shows indications that the GIA signal has not been completely removed, and thus, we cannot interpret the residual strain rates north of this latitude in relation to a possible tectonic signal there. Roughly N-S contraction in the southern states that is present in the GIA model, but not found in the GPS interpolated field, adds additional complications for interpreting the residual field. Thus, better GIA models are needed along with higher-resolution GPS measurements in order to better isolate the tectonic signal.

The warping of the mid-Pliocene Orangeburg scarp that runs parallel to the east coast has been attributed to dynamic topography (Rowley et al., 2013). The distribution of differential horizontal shortening rates across the Piedmont and Coastal plain regions that arises from all models examined (Figure 9) may suggest an additional factor for the warping of the Orangeburg scarp, where uplift may be associated with the dis-

tributed shortening and crustal thickening of a lower crustal ductile zone. Contraction rates in Model 4 (the preferred model) across the Piedmont and Coastal plain regions would yield ~0.1–0.2 mm/year of shortening ($2–4 \times 10^{-10}$ year$^{-1}$ of contractional strain rates). If we take the contractional dilatational strain rates in Model 4, which peak near the North Carolina-Virginia boarder at values of about $4 \times 10^{-10}$ year$^{-1}$, and apply these contractional strain rates over the thickness of the crust (35 km), then a long-term crustal thickening change of 14 m per million years would occur along these coastal regions owing to the long-term shortening. If this thickening is isostatically compensated, it would result in 2.4 m of uplift per million years and an overall warping of about 14 m since early Pliocene between southern South Carolina and northern Virginia. Such a differential uplift is compatible with observed warping of the Orangeburg scarp (Rowley et al., 2013). Thus, distributed crustal shortening and thickening may be an additional factor that has acted, together with dynamic topography changes, to warp the Orangeburg scarp. The remainder of horizontal shortening rates in Model 4 occur across the eastern Tennessee seismic belt (Figure 9d). Measurement of long-term features using geomorphic evidence (Berti et al., 2015) has potential to better constrain long-term rates of shortening.

## 4. Discussion and Conclusion

In this study, we investigate the role of large-scale tectonic stresses, along with first-order lateral strength variations within the lithosphere, in causing intraplate earthquakes in CEUS. Although it is generally agreed that intraplate seismicity is caused by reactivation of preexisting faults, the reason for such reactivation is still not clear. GIA has been argued to be one of the factors for such reactivation in this region (e.g., Mazzotti et al., 2005; Muir-Wood, 2000; Steffen et al., 2014). However, a number of studies have also argued that the GIA effect drops off sharply south of the ice sheet hinge line and thus plays a minimal role in affecting the stress field (James & Bent, 1994; Kreemer et al., 2018; Wu & Johnston, 2000; Zoback, 1992). Also, if the earthquakes were caused by GIA signal, their shortening directions obtained from *P* axes would be in the direction of GIA shortening directions. Instead, the GIA signal is generally orthogonal to the actual directions of shortening that is inferred from the earthquake *P* axes. Furthermore, a GIA-dominated stress field would have the same orientation as the GIA-dominated strain rate field (Figure 3a) with principal axes of compression directed radially outward from the ice sheet. Such a radial pattern does not fit the orientations of the $\sigma_{H\,\max}$ directions from stress inversions. Noting that GIA is a transient ($10^4$–$10^5$ years) response, then the surface strain rates associated with GIA reflect stress rates within the elastic portion of the lithosphere. These GIA-associated stress rates will generally add to or subtract from the total deviatoric stress field (e.g., Muir-Wood, 2000), which we are calculating from GPE gradients and coupled mantle flow. These stress rates from GIA within CEUS are generally contractional, oriented radially outward from the paleo-ice load and typically orthogonal to the NE-SW oriented contraction directions of maximum compressional deviatoric stress. Thus, the GIA-associated stress rates will typically not influence the magnitudes of the $\sigma_{H\,\max}$ directions of total stress in CEUS because they are orthogonal to those directions. It is possible to estimate these GIA related stress rates by assuming an elastic shear modulus for the elastic portion of the lithosphere and multiplying by the strain rates. Assuming incompressible elastic and a shear modulus of $3 \times 10^{10}$ N/m$^2$, the stress rates would be of the order of 60 Pa/year for GIA strain rates of $2 \times 10^{-9}$ year$^{-1}$. This stress rate, when multiplied by the return time of large earthquakes (~$10^3$–$10^4$ years), yields a total stress change that is still small in comparison to the total deviatoric stress magnitudes that are acting long-term (~$5 \times 10^7$ Pa).

We have shown that long wavelength tectonic stresses, namely, the combination of the influence of topography and lithospheric structure, together with coupling with large-scale mantle flow, can match earthquake stress and strain indicators in CEUS and could potentially be responsible for their occurrence. The mantle flow field is influenced primarily by the history of subduction beneath North America (Bunge & Grand, 2000; Forte et al., 2010; Grand et al., 1997; Sigloch & Mihalynuk, 2013). Further refinements in estimated stresses can be obtained by considering new constraints on crustal, upper mantle, and whole mantle structure, provided by EarthScope USArray studies (Biryol et al., 2016; Chen et al., 2016). However, a significant unknown is the rheology and location of other strength contrasts or weak zones within the lithosphere. Our model considers only first-order strength contrasts, such as the large-scale features of craton boundary, zones of accreted Appalachian terranes, and the transition from stretched continental margin to old oceanic lithosphere. We have shown that an order of magnitude strength contrast across these boundaries results in strain rates that are likely too high within the zone of accreted terranes. A factor of 2 reduction in effective viscosity within the zone of accreted Appalachian terranes (Model 4) yields strain rates that are below

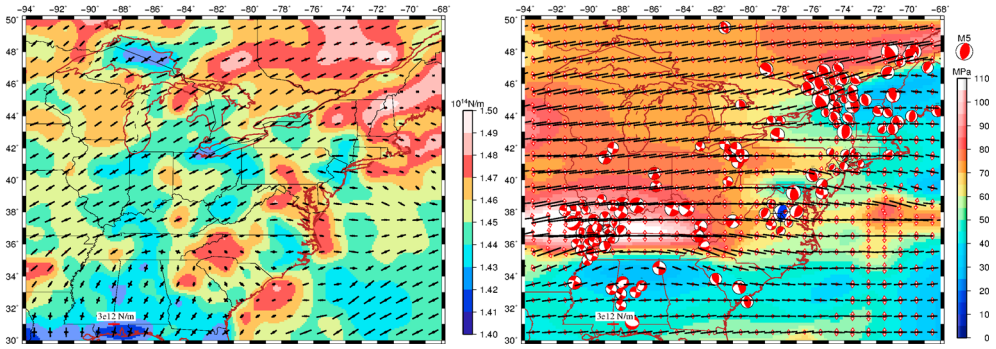


**Figure 10.** (a) Principal axes of deviatoric stresses derived from gravitational potential energy (GPE) variations. (b) Principal axes of deviatoric stresses derived from density-driven mantle convection and their second invariants. Also shown are the focal mechanisms of various earthquakes. Both the models have lateral variations from viscosity Model 3.

the expected upper bound ($1 \times 10^{-9}$ year$^{-1}$). Assuming a 15-km-thick seismogenic layer, we have converted these strain rates to long-term expected seismic moment rates (Holt et al., 1995, 2000; Figure 9e). This is an upper bound on the long-term seismic moment rate because some of the long-term strain rates may be accommodated aseismically. These long-term moment rates translate to a total moment that is equivalent to about three magnitude 7.1 earthquakes over a 300-year period between the regions of 32°N and 51°N and 70–90°W. Such long-term tectonic moment rates predicted by Model 4 (Figure 9e) may be consistent with the observed total moment release over the same interval (Neely et al., 2018).

Although our model produces a reasonable match with $P$ axes of earthquakes as well as with $\sigma_{H\,\max}$ of stress inversions within the New Madrid region (Figures 6 and 7), it does not include a zone of potential lithosphere weakness there, which has been hypothesized to play a significant role in focusing deformation in the New Madrid region (Kenner & Segall, 2000; Liu & Zoback, 1997; Mooney et al., 2012). Other potential regions of lithospheric weakness may also play a role in focusing deformation (Hamburger & Rupp, 1988; Hatcher et al., 2013; Lamontagne et al., 2003; Murphy & Egbert, 2017; Wheeler, 1995). One example is the Mineral, Virginia, earthquake, which occurs within the zone of maximum strain rates, at the boundary between the stiff craton and a weaker intraplate region (Figures 9b and 9c), although Pratt et al. (2015) had argued that the 2011 event ruptured a new fault rather than reactivating an existing structure. Levandowski et al. (2016) argued for a dense lower crust in the New Madrid area that gave rise to high GPE and hence large gravitational stresses. This, in turn, they argued, was responsible for high seismicity rate in the region. However, the GPE derived from the Crust1.0 model does not show any anomalous high values in that region (Figure 10a). On the other hand, stresses derived from density-driven mantle circulation show the highest values in the New Madrid area (Figure 10b) in the presence of lateral viscosity variations, arising from stiff craton adjacent to the weaker zone of accreted Appalachian terranes. The presence of a strong viscosity contrast seems to be focusing the stresses at the boundary of the craton, which could potentially be responsible for high seismicity in the New Madrid area. However, most likely, the model result involving the focusing of stresses in the New Madrid region has a lot to do with where we have placed the craton boundary, which passes through the New Madrid seismic zone. Therefore, this model does not test the possible influences that a potentially weakened lithosphere in the New Madrid region itself (Kenner & Segall, 2000; Liu & Zoback, 1997; Mooney et al., 2012) might have on the stress state.

We tested four viscosity models in order to see what kind of lateral strength variations can explain the focal mechanisms in this region. We saw that a model with a single intraplate viscosity yields a more or less uniform pattern of ENE-WSW directed compressive stress throughout the plate interior. Introduction of strength variations that give rise to a weak region sandwiched between the strong cratonic block to the west and the strong western Atlantic block to the east induces a rotation of the stress axes, which fit the mechanisms of some of the events on the eastern seaboard better but degrade the fit to others. We also compared the predicted stresses with recent stress inversions (Levandowski et al., 2018) and the orientation of the $P$ axes of earthquakes in North America. The statistical analysis provided inconclusive results as to the best intraplate viscosity structure. Our results indicate, however, that the earthquakes result from tectonic effects (GPE differences and coupling with mantle flow). The analysis of GPS data showed that contrac-

tional strain rates are dominated by a GIA signal that yields contraction directions that are oriented radial to the paleo-ice load, and these directions are generally orthogonal to the direction of maximum shortening strain exhibited by earthquakes (ENE to WSW). By subtracting out the theoretical horizontal strain rate field predicted by the ICE-6G model, we conclude that contraction rates from tectonic effects are unlikely to exceed $1 \times 10^{-9}$ year$^{-1}$. This upper bound in strain rate provides a lower bound on the effective viscosity of the craton and adjacent zones of accreted Appalachian terranes. Further work is needed to investigate the importance of other lateral strength contrasts, the magnitude of these contrasts, along with the implications for expected long-term permanent deformation and seismic moment release.

**Acknowledgments**
We thank Will Levandowski, the Associate Editor, and an anonymous reviewer whose suggestions have improved the manuscript. Figures were prepared using GMT 4.5.8 by P. Wessel and W. F. Smith. This work was partly supported by NSF grant EAR-1358613 and NASA award NNX16AL18G to W. E. H. The compilation of the earthquake data is included in Table 1, whereas the stress inversion data are downloaded from https://www.nature.com/articles/s41561-018-0120-x#Sec16 website.

## References

Amante, C., & Eakins, B. W. (2009). ETOPO1 1 arc-minute global relief model: Procedures, data sources and analysis. *NOAA Technical Memorandum NESDIS NGDC*, *24*, 19.

Argus, D. F., Peltier, W. R., Drummond, R., & Moore, A. W. (2014). The Antarctica component of postglacial rebound model ICE-6G_C (VM5a) based on GPS positioning, exposure age dating of ice thicknesses, and relative sea level histories. *Geophysical Journal International*, *197*, 537–563.

Beavan, J., & Haines, J. (2001). Contemporary horizontal velocity and strain rate fields of the Pacific-Australian plate boundary zone through New Zealand. *Journal of Geophysical Research*, *106*, 741–770.

Becker, T. W., Lowry, A. R., Faccenna, C., Schmandt, B., Borsa, A., & Yu, C. (2015). Western US intermountain seismicity caused by changes in upper mantle flow. *Nature*, *524*, 458–461.

Bent, A. (1995). A complex double-couple source mechanism for the Ms 7.2 1929 Grand Banks earthquake. *Bulletin of the Seismological Society of America*, *85*, 1003–1020.

Bent, A. (1996). Source parameters of the damaging Cornwall-Massena earthquake of 1944 from regional waveforms. *Bulletin of the Seismological Society of America*, *86*, 489–497.

Bent, A. (2002). The 1933 Ms = 7.3 Baffin Bay earthquake. *Geophysical Journal International*, *150*, 724–736.

Berti, C., Pazzaglia, F., Meltzer, A. S., & Harrison, R. J. (2015). Geomorphic evidence for persistent, cumulative deformation of the Virginia Piedmont in the vicinity of the 23 August 2011 Mineral earthquake. In J. W. Horton Jr, M. C. Chapman, & R. A. Green (Eds.), *The 2011 Mineral, Virginia, earthquake, and its significance for seismic hazards in eastern North America* (Vol. 509, pp. 377–390). Boulder, CO: Geological Society of America Special Paper.

Bird, P., Kreemer, C., & Holt, W. E. (2010). A long-term forecast of shallow seismicity based on the global strain rate map. *Seismological Research Letters*, *81*, 184–194. https://doi.org/10.1785/gssrl.81.2.184

Bird, P., & Liu, Z. (2007). Seismic hazard inferred from tectonics: California. *Seismological Research Letters*, *78*, 37–48.

Biryol, C. B., Wagner, L. S., Fischer, K. M., & Hawman, R. B. (2016). Relationship between observed upper mantle structures and recent tectonic activity across the Southeastern United States. *Journal of Geophysical Research: Solid Earth*, *121*, 3393–3414. https://doi.org/10.1002/2015JB012698

Bunge, H. P., & Grand, S. (2000). Mesozoic plate-motion history below the northeast Pacific Ocean from seismic images of the subducted Farallon slab. *Nature*, *405*, 337–340.

Burgmann, R., & Dresen, G. (2008). Rheology of the lower crust and upper mantle: Evidence from rock mechanics, geodesy, and field observations. *Annual Review of Earth and Planetary Sciences*, *36*, 531–567.

Calais, E., Han, J. Y., DeMets, C., & Noquet, J. M. (2006). Deformation of the North American plate interior from a decade of continuous GPS measurements. *Journal of Geophysical Research*, *111*, B06402. https://doi.org/10.1029/2005JB004253

Chen, C., Gilbert, H., Andronicos, C., Hamburger, M. W., Larson, T., Marshak, S., et al. (2016). Shear velocity structure beneath the central United States: Implications for the origin of the Illinois Basin and intraplate seismicity. *Geochemistry, Geophysics, Geosystems*, *17*, 1020–1041. https://doi.org/10.1002/2015GC006206

Cook, F. A., & Oliver, J. E. (1981). The late precambrian-early Paleozoic continental edge in the Appalachian orogen. *American Journal of Science*, *281*, 993–1008.

Du, W., Kim, W., & Sykes, L. R. (2003). Earthquake source parameters and state of stress for the Northeastern United States and Southeastern Canada from analysis of regional seismograms. *Bulletin of the Seismological Society of America*, *93*, 1633–1648.

Ebel, J. E. (2009). Analysis of aftershock and foreshock activity in stable continental regions: Implications for aftershock forecasting and the hazard of strong earthquakes. *Seismological Research Letters*, *80*, 977–983.

Finzel, E., Flesch, L. M., Ridgway, K. D., Holt, W. E., & Ghosh, A. (2015). Surface motions and intraplate continental deformation in Alaska driven by mantle flow. *Geophysical Research Letters*, *42*, 4350–4358. https://doi.org/10.1002/2015GL063987

Flesch, L. M., Haines, A. J., & Holt, W. E. (2001). Dynamics of the India-Eurasia collision zone. *Journal of Geophysical Research*, *106*, 16,435–16,460.

Forte, A. M., Mitrovica, J. X., Moucha, R., Simmons, N. A., & Grand, S. P. (2007). Descent of the ancient Farallon slab drives localized mantle flow below the New Madrid seismic zone. *Geophysical Research Letters*, *34*, L04308. https://doi.org/10.1029/2006GL027895

Forte, A., Moucha, R., Simmons, N., Grand, S., & Mitrovica, J. (2010). Deep-mantle contributions to the surface dynamics of the North American continent. *Tectonophysics*, *481*, 3–15. https://doi.org/10.1016/j.tecto.2009.06.010

Gallen, S. F., & Thigpen, J. R. (2018). Lithologic controls on focused erosion and intraplate earthquakes in the eastern Tennessee seismic zone. *Geophysical Research Letters*, *45*, 9569–9578. https://doi.org/10.1029/2018GL079157

Gangopadhyay, A., & Talwani, P. (2003). Symptomatic features of intraplate earthquakes. *Seismological Research Letters*, *74*, 863–883.

Ghosh, A., Becker, T. W., & Humphreys, E. (2013). Dynamics of the North American continent. *Geophysical Journal International*, *194*, 651–669.

Ghosh, A., & Holt, W. E. (2012). Plate motions and stresses from global dynamic models. *Science*, *335*, 838–843. https://doi.org/10.1126/science.1214209

Ghosh, A., Holt, W. E., & Flesch, L. M. (2009). Contribution of gravitational potential energy differences to the global stress field. *Geophysical Journal International*, *179*, 787–812.

Ghosh, A., Holt, W. E., Haines, A. J., & Flesch, L. M. (2006). Gravitational potential energy of the Tibetan Plateau and the forces driving the Indian plate. *Geology*, *34*, 321–324.

Ghosh, A., Holt, W. E., & Wen, L. (2013). Predicting the lithospheric stress field and plate motions by joint modeling of lithosphere and mantle dynamics. *Journal of Geophysical Research: Solid Earth*, *118*, 346–368. https://doi.org/10.1029/2012JB009516

Ghosh, A., Holt, W. E., Wen, L., Haines, A. J., & Flesch, L. M. (2008). Joint modeling of lithosphere and mantle dynamics elucidating lithosphere-mantle coupling. *Geophysical Research Letters*, *35*, L16309. https://doi.org/10.1029/2008GL034365

Grand, S. P., van der Hilst, R. D., & Widiyantoro, S. (1997). Global seismic tomography: A snapshot of convection in the Earth.

Haines, A. J., & Holt, W. E. (1993). A procedure for obtaining the complete horizontal motions within zones of distributed deformation from the inversion of strain rate data. *Journal of Geophysical Research*, *98*, 12,057–12,082.

Hamburger, M. W., & Rupp, J. A. (1988). The June 1987 Southeastern Illinois earthquake: Possible tectonism associated with the La Salle anticlinal belt. *Seismological Research Letters*, *59*, 151–157.

Hatcher, R. D., Vaughn, J. D., & Obermeier, S. F. (2013). Large earthquake paleoseismology in the East Tennessee seismic zone: Results of an 18-month pilot study. *Geological Society of America Special Paper*, *493*, 111–142.

Hirschberg, H. P., Lamb, S., & Savage, M. K. (2018). Strength of an obliquely convergent plate boundary: Lithospheric stress magnitudes and viscosity in New Zealand. *Geophysical Journal International*, *216*, 1005–1024.

Hirth, G. (2002). Laboratory constraints on the rheology of the upper mantle. *Reviews in Mineralogy and Geochemistry*, *51*, 97–120.

Holt, W. E., Chamot-Rooke, N., Pichon, X. L., Haines, J., Shen-Tu, B., & Ren, J. (2000). The velocity field in Asia inferred from Quaternary fault slip rates and GPS observations. *Journal of Geophysical Research*, *105*, 19,185–19,209.

Holt, W. E., Li, M., & Haines, A. J. (1995). Earthquake strain rates and instantaneous relative motions within central and East Asia. *Geophysical Journal International*, *122*, 569–593.

Horner, R. B., Stevens, A. E., Hasegawa, H. S., & Leblanc, G. (1978). Focal parameters of the July 12, 1975 Maniwaki, Quebec earthquake—An example of intraplate seismicity in eastern Canada. *Bulletin of the Seismological Society of America*, *68*, 619–640.

Horton, J. W., Chapman, M. C., & Green, R. A. (2015). The 2011 Mineral, Virginia, earthquake, and its significance for seismic hazards in eastern North America. In J. W. Horton Jr, M. C. Chapman, & R. A. Green (Eds.), *The 2011 Mineral, Virginia, earthquake, and its significance for seismic hazards in eastern North America* (Vol. 509, pp. 1–25). Boulder, CO: Geological Society of America Special Paper.

Horton, S. P., Kim, W., & Withers, M. (2005). The 6 June 2003 Bardwell, Kentucky, earthquake sequence: Evidence for a locally perturbed stress field in the Mississippi Embayment. *Bulletin of the Seismological Society of America*, *95*, 431–445.

Hough, S. (2004). Scientific overview and historical context of the 1811-1812 New Madrid earthquake sequence. *Annals of Geophysics*, *47*, 523–537.

Hough, S. E., & Page, M. (2011). Toward a consistent model for strain accrual and release for the New Madrid Seismic Zone, central United States. *Journal of Geophysical Research*, *116*, B03311. https://doi.org/10.1029/2010JB007783

Hughes, K. S., Hibbard, J. P., & Bohnenstiehl, D. R. (2015). Relict paleozoic faults in the epicentral area of the 23 August 2011 central Virginia earthquake: Assessing the relationship between preexisting strain and modern seismicity. In J. W. Horton Jr, M. C. Chapman, & R. A. Green (Eds.), *The 2011 Mineral, Virginia, earthquake, and its significance for seismic hazards in eastern North America* (Vol. 509, pp. 331–344). Boulder, CO: Geological Society of America Special Paper.

Jackson, J., McKenzie, D., Priestley, K., & Emmerson, B. (2008). New views on the structure and rheology of the lithosphere. *Journal of the Geological Society*, *165*, 453–465.

James, T. S., & Bent, A. L. (1994). A comparison of eastern North American seismic strain-rates to glacial rebound strain-rates. *Geophysical Research Letters*, *21*, 2127–2130.

Jay, C., Flesch, L. M., & Bendick, R. O. (2018). Kinematics and dynamics of the Pamir, Central Asia: Quantifying the roles of continental subduction in force balance. *Journal of Geophysical Research: Solid Earth*, *123*, 8161–8179. https://doi.org/10.1029/2018JB015615

Kagan, Y. Y., & Jackson, D. D. (1994). Long-term probabilistic forecasting of earthquakes. *Journal of Geophysical Research*, *99*, 13,685–13,700.

Keller, G. R., & Hatcher, R. D. (1999). Some comparisons of the structure and evolution of the southern Appalachian–Ouachita orogen and portions of the Trans-European Suture Zone region. *Tectonophysics*, *314*, 43–68.

Kenner, S. J., & Segall, P. (2000). A mechanical model for intraplate earthquakes: Application to the New Madrid seismic zone. *Science*, *289*, 2329–2332.

Kim, W. (2003). The 18 June 2002 Caborn, Indiana, Earthquake: Reactivation of ancient rift in the Wabash Valley seismic zone? *Bulletin of the Seismological Society of America*, *93*, 2201–2211.

Kim, W., & Chapman, M. (2005). The 9 December 2003 central Virginia earthquake sequence: A compound earthquake in the central Virginia seismic zone. *Bulletin of the Seismological Society of America*, *95*, 2428–2445.

Kim, W., Dineva, S., Ma, S., & Eaton, D. (2006). The 4 August 2004, Lake Ontario, earthquake. *Seismological Research Letters*, *77*, 65–73.

Klein, E. C., Flesch, L. M., Holt, W. E., & Haines, A. J. (2009). Evidence of long-term weakness on seismogenic faults in western North America from dynamic modeling. *Journal of Geophysical Research*, *114*, B03402. https://doi.org/10.1029/2007JB005201

Kohlstedt, D. L., Evans, B., & Mackwell, S. J. (1995). Strength of the lithosphere: Constraints imposed by laboratory experiments. *Journal of Geophysical Research*, *100*, 17,587–17,602.

Kreemer, C., Blewitt, G., & Klein, E. C. (2014). A geodetic plate motion and Global Strain Rate Model. *Geochemistry, Geophysics, Geosystems*, *15*, 3849–3889. https://doi.org/10.1002/2014GC005407

Kreemer, C., Hammond, W. C., & Blewitt, G. (2018). A robust estimation of the 3-D intraplate deformation of the North American plate from GPS. *Journal of Geophysical Research: Solid Earth*, *123*, 4388–4412. https://doi.org/10.1029/2017JB015257

Kreemer, C., Lavallee, D. A., Blewitt, G., & Holt, W. E. (2006). On the stability of a geodetic no-net-rotation frame and its implication for the International Terrestrial Reference Frame. *Geophysical Research Letters*, *33*, L17306. https://doi.org/10.1029/2006GL027058

Lamontagne, M., Keating, P., & Perrault, S. (2003). Seismotectonic characteristics of the Lower St. Lawrence Seismic Zone, Quebec: Insights from geology, magnetics, gravity, and seismics. *Canadian Journal of Earth Sciences*, *40*, 317–336.

Levandowski, W., Boyd, O. S., & Ramirez-Guzman, L. (2016). Dense lower crust elevates long-term earthquake rates in the New Madrid seismic zone. *Geophysical Research Letters*, *43*, 8499–8510. https://doi.org/10.1002/2016GL070175

Levandowski, W., Herrmann, R. B., Briggs, R., Boyd, O., & Gold, R. (2018). An updated stress map of the continental United States reveals heterogeneous intraplate stress. *Nature Geoscience*, *11*, 433–437. https://doi.org/10.1038/s41561-018-0120-x

Levandowski, W., Zellman, M., & Briggs, R. (2017). Gravitational body forces focus North American intraplate earthquakes. *Nature Communications*, *8*, 14314. https://doi.org/10.1038/ncomms14314

Li, Q., Liu, M., Zhang, Q., & Sandvol, E. (2007). Stress evolution and seismicity in the central-eastern USA: Insights from geodynamic modeling. In S. Stein, & S. Mazzotti (Eds.), *Continental Intraplate Earthquakes: Geological Society of America Special Paper* (Vol. 425, pp. 149–166). Geological Society of America.

Lithgow-Bertelloni, C., & Guynn, J. H. (2004). Origin of the lithospheric stress field. *Journal of Geophysical Research*, *109*, B01408. https://doi.org/10.1029/2003JB002467

Liu, L., & Gao, S. (2018). Lithospheric layering beneath the contiguous United States constrained by S-to-P receiver functions. *Earth and Planetary Science Letters*, *495*, 79–86.

Liu, M., & Stein, S. (2016). Mid-continental earthquakes: Spatiotemporal occurrences, causes, and hazards. *Earth-Science Reviews*, *162*, 364–386.

Liu, L., & Zoback, M. D. (1997). Lithospheric strength and intraplate seismicity in the New Madrid seismic zone. *Tectonophysics*, *16*, 585–595.

Ma, S., Eaton, D. W., & Adams, J. (2008). Intraplate seismicity of a recently deglaciated shield terrane: A case study from northern Ontario, Canada. *Bulletin of the Seismological Society of America*, *98*, 2828–2848.

Mazzotti, S., James, T. S., Henton, J., & Adams, J. (2005). GPS crustal strain, postglacial rebound, and seismic hazard in eastern North America: The Saint Lawrence valley example. *Journal of Geophysical Research*, *110*, B11301. https://doi.org/10.1029/2004JB003590

Mazzotti, S., & Townend, J. (2010). State of stress in central and eastern North American seismic zones. *Lithosphere*, *2*, 76–83. https://doi.org/10.1130/L65.1

McKenzie, D. P. (1969). The relation between fault plane solutions for earthquakes and the directions of the principal stresses. *Bulletin of the Seismological Society of America*, *59*, 591–601.

Mooney, W. D., Ritsema, J., & Hwang, Y. K. (2012). Crustal seismicity and the earthquake catalog maximum moment magnitude (Mcmax) in stable continental regions (SCRs): Correlation with the seismic velocity of the lithosphere. *Earth and Planetary Science Letters*, *357-358*, 78–83.

Muir-Wood, R. (2000). Deglaciation seismotectonics: A principal influence on intraplate seismogenesis at high latitudes. *Quaternary Science Reviews*, *19*, 1399–1411.

Murphy, B. S., & Egbert, G. D. (2017). Electrical conductivity structure of southeastern North America: Implications for lithospheric architecture and Appalachian topographic rejuvenation. *Earth and Planetary Science Letters*, *462*, 66–75.

Naliboff, J. B., Conrad, C. P., & Lithgow-Bertelloni, C. (2009). Modification of the lithospheric stress field by lateral variations in plate-mantle coupling. *Geophysical Research Letters*, *36*, L22307. https://doi.org/10.1029/2009GL040484

Naliboff, J. B., Lithgow-Bertelloni, C., Ruff, L. J., & Koker, N. J. (2012). The effects of lithospheric thickness and density structure on Earth's stress field. *Geophysical Journal International*, *188*, 1–17.

Neely, J. S., Stein, S., Merino, M., & Adams, J. (2018). Have we seen the largest earthquakes in eastern North America. *Physics of the Earth and Planetary Interiors*, *284*, 17–27.

Peltier, W. R., Argus, D. F., & Drummond, R. (2015). Space geodesy constrains ice age terminal deglaciation: The global ICE-6G_C (VM5a) model. *Journal of Geophysical Research: Solid Earth*, *119*, 450–487. https://doi.org/10.1002/2014jb011176

Pratt, T. L., Coruh, C., Costain, J. K., & Glover III, L. (1988). A geophysical study of the Earth's crust in central Virginia: Implications for Appalachian crustal structure. *Journal of Geophysical Research*, *93*, 6649–6667.

Pratt, T. L., Horton Jr, J. W. H., Spears, D. B., Gilmer, A. K., & McNamara, D. E. (2015). The 2011 Virginia Mw 5.8 earthquake: Insights from seismic reflection imaging into the influence of older structures on eastern U.S. seismicity The 2011 Virginia Mw 5.8 earthquake: Insights from seismic reflection imaging into the influence of older structures on eastern U.S. seismicity. In J. W. Horton Jr, M. C. Chapman, & R. A. Green (Eds.), *The 2011 Mineral, Virginia, earthquake, and its significance for seismic hazards in eastern North America* (Vol. 509, pp. 258–294). Colorado: Geological Society of America Special Paper.

Rowley, D. B., Forte, A. M., Moucha, R., Mitrovica, J. X., Simmons, N. A., & Grand, S. P. (2013). Dynamic topography change of the eastern United States since 3 million years ago. *Science*, *340*, 156–1563. https://doi.org/10.1126/science.1229180

Sbar, M. L., Jordan, R. J., Stephens, C. D., Pickett, T. E., Woodruff, K. D., & Sammis, C. G. (1975). The Delaware-New Jersey earthquake of February 28, 1973. *Bulletin of the Seismological Society of America*, *65*, 85–92.

Schulte, S., & Mooney, W. D. (2005). An updated global earthquake catalogue for stable continental regions: Reassessing the correlation with ancient rifts. *Geophysical Journal International*, *161*, 707–721.

Sella, G., Stein, S., Dixon, T., Craymer, M., James, T., & Mazzotti, S. (2007). Observations of glacial isostatic adjustment in stable North America with GPS. *Geophysical Research Letters*, *34*, L02306. https://doi.org/10.1029/2006GL027081

Shen, W., & Ritzwoller, M. H. (2016). Crustal and uppermost mantle structure beneath the United States. *Journal of Geophysical Research: Solid Earth*, *121*, 4306–4342. https://doi.org/10.1002/2016JB012887

Sigloch, K., & Mihalynuk, M. G. (2013). Intra-oceanic subduction shaped the assembly of Cordilleran North America. *Nature*, *496*, 50–57. https://doi.org/10.1038/nature12019

Steffen, R., Wu, P., Steffen, H., & Eaton, D. W. (2014). The effect of Earth rheology and ice-sheet size on fault slip and magnitude of postglacial earthquakes. *Earth and Planetary Science Letters*, *388*, 71–80.

Stein, S., Cloetingh, S., Sleep, N. H., & Wortel, R. (1989). Passive margin earthquakes, stresses and rheology. In S. Gregerson, & P. Basham (Eds.), *Earthquakes at North-Atlantic passive margins: Neotectonics and postglacial rebound* (pp. 231–260). Dordecht: Kluwer.

Sykes, L. (1978). Intraplate seismicity, reactivation of preexisting zones of weakness, alkaline magmatism, and other tectonism postdating continental fragmentation. *Reviews of Geophysics*, *16*, 621–688.

Wang, X., Holt, W. E., & Ghosh, A. (2015). Joint modeling of lithosphere and mantle dynamics: Evaluation of constraints from global tomography models. *Journal of Geophysical Research: Solid Earth*, *120*, 8633–8655. https://doi.org/10.1002/2015JB012188

Wen, L., & Anderson, D. L. (1997). Slabs, hotspots, cratons and mantle convection revealed from residual seismic tomography in the upper mantle. *Physics of the Earth and Planetary Interiors*, *99*, 131–143.

Wheeler, R. L. (1995). Earthquakes and the cratonward limit of Iapetan faulting in eastern North America. *Geology*, *23*, 105–108.

Williams, H., & Hatcher, R. D. (1982). Suspect terranes and accretionary history of the Appalachian orogen. *Geology*, *10*, 530–536.

Wilson, T. J. (1965). A new class of faults and their bearing on continental drift. *Nature*, *207*, 343–347. https://doi.org/10.1038/207343a0

Wolin, E., Stein, S., Pazzaglia, F., Meltzer, A., & Kafka, A. (2012). Mineral, Virginia, earthquake illustrates seismicity of a passive-aggressive margin. *Geophysical Research Letters*, *39*, L02305. https://doi.org/10.1029/2011GL050310

Wu, P., & Johnston, P. (2000). Can deglaciation trigger earthquakes in N. America? *Geophysical Research Letters*, *27*, 1323–1326. https://doi.org/10.1029/1999GL011070

Yang, J., & Aggarwal, Y. P. (1981). Seismotectonics of Northeastern United States and Adjacent Canada. *Journal of Geophysical Research*, *86*, 4981–4998.

Yuan, H., & Romanowicz, B. (2010). Lithospheric layering in the North American craton. *Nature*, *466*, 1063–1069. https://doi.org/10.1038/nature09332

Zoback, M. L. (1992). First and second order patterns of stress in the lithosphere: The World Stress Map Project. *Journal of Geophysical Research*, *102*, 11,703–11,728.
Zoback, M. L., & Richardson, R. M. (1996). Stress perturbation associated with the Amazonas and other ancient continental rifts. *Journal of Geophysical Research*, *101*, 5459–5475.
Zoback, M. L., & Zoback, M. D. (1980). State of stress in the conterminous United States. *Journal of Geophysical Research*, *85*, 6113–6156.
Zoback, M. D., & Zoback, M. L. (1981). State of stress and intraplate earthquakes in the United States. *Science*, *213*, 96–104.